Vibration analysis of a dual-rotor-bearing-double casing system with pedestal looseness and multi-stage turbine blade-casing rub

Yang Yang[1*], Huajiang Ouyang[2], Yiren Yang[1], Dengqing Cao[3], Kai Wang[4]

1. School of Mechanics and Engineering, Southwest Jiaotong University, Chengdu 610031, China

2. Centre for Engineering Dynamics, School Engineering, University of Liverpool, Liverpool L69 3GH, UK

3. School of Astronautics, Harbin Institute of Technology, PO Box 137, Harbin 150001, China

4. State Key Laboratory of Advanced Design and Manufacturing for Vehicle Body, Hunan University, Changsha 410082, China

Abstract: Pedestal looseness and rotor-stator rub are two common faults in rotating machines. To increase the thrust-weight ratio and enhance fuel efficiency of aero engines, the structural design of a dual-rotor system has to address these two kinds of common faults. The aim of this paper is to gain insight into the vibration behaviours of a dual-rotor system with pedestal looseness and rotor-stator rub. Firstly, a dual-rotor-bearing-double casing system is modelled. After that, considering the effects of two disc imbalances, and pedestal looseness which exists in high pressure rotor, the rub-impact fault between the multi-stage turbine blades and the multi-layer casings is further introduced to the system. In combination with the distribution of soft and hard coatings, the impact stiffness of the rub-impact model is adjusted accordingly. Then an experimental study is performed on a dual-rotor test rig for verifying the validity of the theoretical model and revealing the dynamic responses at different rotor speed ratio. Finally, taking the stiffness of loosened pedestals, disc eccentricities, speed ratio, and initial gap as the key parameters, the potential effects of pedestal looseness and rub-impact on the dynamic characteristics of the dual-rotor system are investigated in detail.

Key words: Dual-rotor system, pedestal looseness, rub-impact, coating, dynamic characteristics

1. Introduction

The thrust has always been towards attaining an optimum and compact engine structure to realize minimum weight for given engine rating and minimum sensitivity to unbalance [1]. A dual-spool arrangement is a common configuration adopted in aero engines to pursue higher thrust and better aerodynamic stability [2]. Being distinct from a single rotor, a dual-rotor system contains two coaxial spools, and their rotational speeds may be the same or different. More importantly, the inclusion of a special inter-shaft bearing connects the inner rotor with the outer rotor facilitates cross-excitation. This design trend of moving from a single rotor system to a dual-rotor system requires more complex theoretical models, in which more factors would be considered and better captured.

To lower vibration noise and enhance overall performance of rotating machines, it is essential for engineers to determine dynamic characteristics of dual-rotor systems in advance. Ferraris et al. [3]

analysed the natural characteristics of a non-symmetric coaxial co- or counter-rotational rotor and discussed the vibration responses due to mass imbalance. Childs [4] proposed a transient modal simulation model for a typical two-spool jet engine configuration, which included a low-speed rotor, a high-speed rotor and a support structure. Then he predicted the vibration responses of the model by numerical simulation. Using the harmonic balance-alternating frequency/time domain (HB-AFT) method, Hou et al. [5] focused on the primary resonance analysis of a dual-rotor system having two unbalance excitations of different rotational speeds. Li et al. [6] evaluated two model truncation schemes with regard to the critical speed, stability, and unbalance response of a two-spool gas turbine engine. Meanwhile, the numbers of modes required to yield acceptable accuracy in these cases were determined as well. Guskov et al. [7] carried out an experimental study of a dual-rotor test rig and measured the vibration responses in the process of rub-ups. The influences of the rotation of each rotor on the critical speed and the associated amplitude were studied in [7]. Anilkumar et al. [8] investigated the dynamics of a rigid body with two attached rotors and used the Floquet theory to identify the stability boundaries. Overall, the above research mainly concentrates on the natural characteristics (i.e., critical speed, vibration mode) and whirling motion of dual-rotor systems.

In the past years, fault analysis of dual-rotor systems has attracted a huge amount of interest as well. Yu et al. [9] studied the dynamic responses of a dual-rotor system at instantaneous and windmilling states when the event of fan blade-out happened. Aiming at analyzing a dual-rotor gas turbine engine supported on bearings and squeeze film dampers, Sun et al. [10] presented an approach for blade loss simulation including thermal growth effects. Lu et al. [11] investigated the nonlinear vibration of a dual-rotor system with a transverse breathing crack in the hollow shaft of the high-pressure rotor. Wang et al. [12] set up a dynamic model for a dual-rotor system with inter-shaft bearings and then revealed the vibration characteristics corresponding to the unbalance-misalignment coupled fault. Taking a dual-rotor system as the object, Yang et al. [13, 14] simulated the dynamic behaviours of the system with fixed-point rub and observed the combination forms in the frequency domain.

In the aviation industry, blade-casing rub is usually caused by misalignment, imbalance, oil whipping and pedestal looseness [15-19]. Although rub-impact is only a secondary fault, it could accelerate erosion and thermal fatigue. Furthermore, rub-impact may even cause the blades to break, the casing to fracture and other catastrophic failures in the worst cases [20, 21]. Based on a numerical model and an experimental set-up, Torkhani et al. [22] investigated the partial rub of a rotor due to contact with a non-rotating obstacle. Tofighi-Niaki et al. [23] employed mixed lubrication theory along with elastic-plastic asperity contact model to simulate the nonlinear dynamics of a flexible rotor system with rub-impact. Roques et al. [24] investigated the speed transients of a system with rotor-to-stator rubbing caused by an accidental blade-off imbalance. Using time frequency techniques, the fault identification problems, such as misalignment, crack and rub, were solved in [25]. Weaver et al. [26] analytically examined a three-disk rotor for nonlinear behaviour due to an unbalance-driven rub. A mathematical model to investigate the dynamics of a Jeffcott rotor having intermittent contact with a stator was presented in [27] and the parameter variations of the rotor speed and the mass ratio of the stator and the rotor were examined. Shaw et al.

[28] performed an analysis of sustained bouncing phenomenon of rotating shafts under the rotor-stator contact. Based on a survey of the literature, it can be seen that the main concern is the rub-impact between the single-turbine and the casing. However, rub-impact between multi-stage turbine blades and multi-layer casings has been rarely studied. According to the actual needs in practice, rub-impact occurring in a multi-stage structure must be understood through an in-depth study.

As one of the common faults in rotating machines, pedestal looseness could reduce the elastic constraint stiffness of a pedestal and can cause violent vibration of a rotor system, which greatly increases the possibility of rub-impact. In [30], a nonlinear mathematical model was developed for a rotor-bearing system including pedestal looseness. At the same time, the nonlinear dynamic characteristics were discussed by a nonlinear fitting method under different looseness clearances. Based on an elastic half space soil model, Ruhl et al. [31] determined the unbalanced responses of a large rotor-pedestal-foundation. Qin et al. [32] analysed the time-varying stiffness of a connective structure with bolt loosening by means of a three-dimensional (3D) nonlinear finite element model. Nataraj et al. [33] studied the dynamic response of a rotor-bearing system with angular misalignment and pedestal looseness. Although much progress has been made to analyse the pedestal looseness, most of the previous studies are on single rotor systems.

Up to now, the blade-casing rub and imbalance excitation have been studied in depth. However, previous investigations on the pedestal looseness are mainly limited to simple single rotor systems, which are obviously different from the actual rotating machines. Actually, it is of practical significance for diagnosing faults and ensuring stability to carry out the prediction of the dynamic responses of a complete aero-engine subjected to pedestal looseness fault.

This paper aims at revealing the vibration characteristics of a complete aero-engine system having pedestal looseness and multi-stage turbine blade-casing rub, a dual-rotor-bearing-double casing dynamic model is set up and the influences of the pedestal looseness are studied emphatically. The structure of the paper is organized as follows: Firstly, the dynamic modelling of a complete aero-engine system, including dual-rotor part, bearings, pedestals, inner casing, outer casing, and blade-casing rub, is set up in Section 2. Next, different types of vibration behaviours of a dual-rotor test rig are reported and in particular the beat vibration and frequency spectrum for identifying rub-impact are analysed in Section 3. Moreover, the effects of pedestal looseness and rub-impact on the dynamic characteristics of the dual-rotor system are revealed in Section 4, in which the loosening pedestal stiffness, disc eccentricities, speed ratio, and initial gap are considered as the key parameters. Finally, some conclusions are summarized in Section 5.

2. Dynamic modelling

In order to predict vibration behaviours of an aero-engine system with both pedestal looseness and rub-impact faults, a complete dual-rotor dynamic model is established in this paper. According to [34], three main modes of rotor vibrations – lateral, torsional and axial modes – may be present in the actual operation of a rotating machine. Among these modes, the lateral modes are of the greatest concern.

A schematic of a dual-rotor-bearing-double casing system capable of lateral vibration is shown in Fig. 1. This complicated integrated system may be divided into four subsystems, including low pressure rotor (LP rotor), high pressure rotor (HP rotor), inner casing and outer casing. In addition, these four subsystems are coupled by the rolling bearings and pedestals. In many cases, under the influence of high frequency excitation, the looseness fault is more likely to occur in the HP rotor. Therefore, a looseness fault is assumed to happen at the one of pedestals of the HP rotor in this paper. In particular, an inter-shaft bearing is installed on the HP turbine disc for coupling the LP rotor and the HP rotor.

For each rotor subsystem, two discs (i.e., compressor disc and turbine disc) with eight straight blades are mounted on the uniform elastic shaft. The inner casing and the outer casing are connected by elastic rods, and the outer casing is supported on the foundation. In the process of modelling, some assumptions are made as follows:

(1) The two rotating shafts are considered as Rayleigh beams, in which the shear effects and the torsion are not considered.

(2) All the discs are assumed to be rigid and their deformations are ignored.

(3) Both inner casing and outer casing are simplified to two lumped mass blocks.

(4) According to a real aero engine device in which the stiffness of blades is much larger than that of the flexible shafts, the elastic deformations of the blades are ignored.

(5) All identical blades are rigidly installed on the discs and the blade-loss event never happens.

(6) The balls of the bearing model are only rolling and the bearing deformation is mainly contact deformation between the rolling balls and the raceway.

(7) The mass eccentricity of the LP turbine disc keeps the same as that of the HP turbine disc.

(8) The effects of thermal and friction torque in rub-impact are ignored.
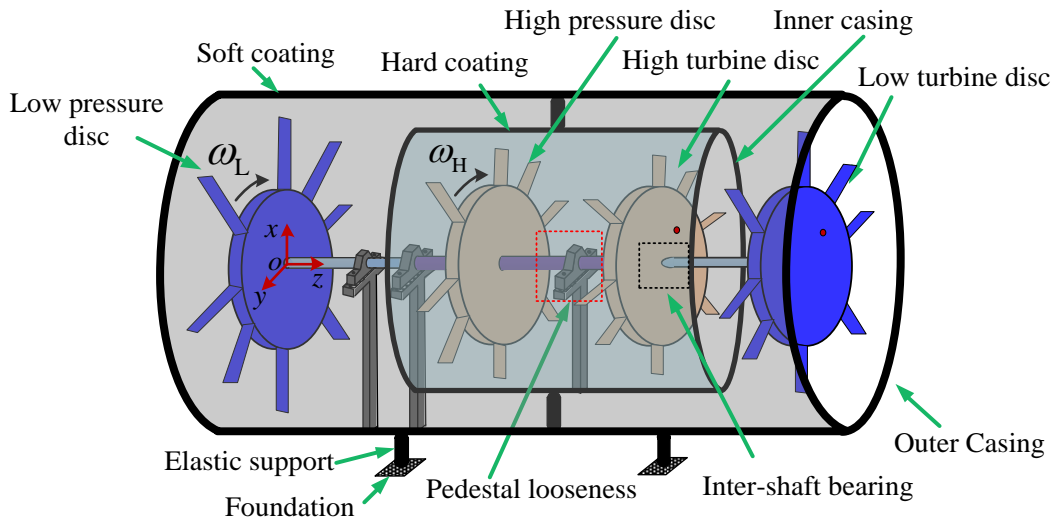

Fig. 1 Schematic diagram of a dual-rotor-bearing-double casing system.

According to the modelling method reported in [35] and the above assumptions, a mathematic model of the dual-rotor-bearing-double casing system is shown in Fig. 2. It can be seen that the elastic rods are modelled as the linear springs and the viscous dampers. The global coordinate system is $o-xyz$, which is fixed to the Earth. Due to the existence of two mass eccentricities, the dual-rotor

system is subjected to two imbalance forces and the excitation frequencies of the two imbalance forces may be the same or not.

In order to achieve gas path sealing, oxidation and corrosion control, coatings have been applied to the surfaces various components [36]. Fig. 2 illustrates that soft coatings are used in the LP rotor and hard coatings are used in the HP rotor. Moreover, a nonlinear spring and a nonlinear viscous damper are introduced to the mathematic model for describing the pedestal looseness. The specific expressions of the nonlinear spring and the nonlinear damping will be given later.
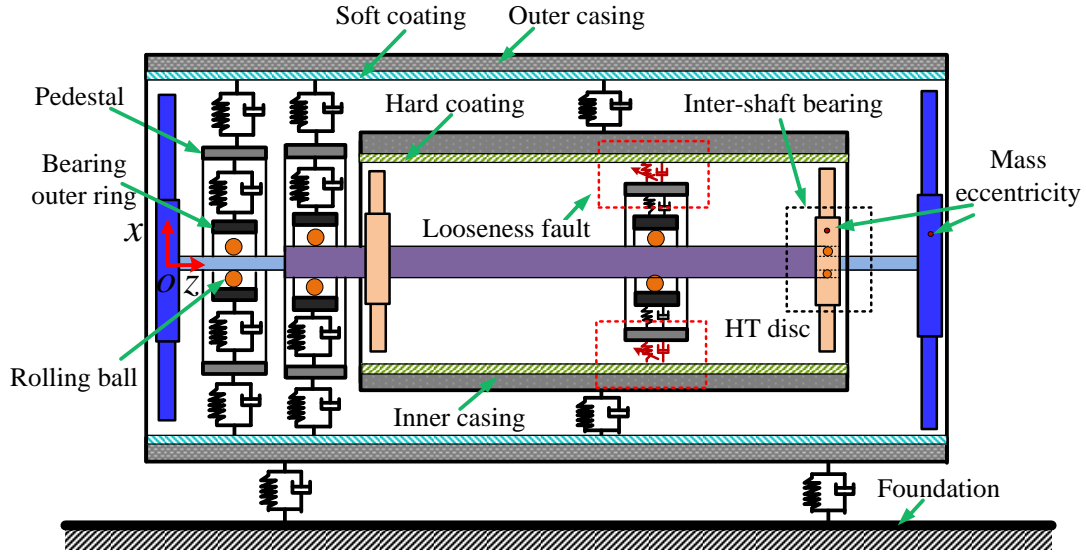
Fig. 2 Mathematic model of a dual-rotor-bearing-double casing system.

2.1 Finite element discretization of dual rotor part

Firstly, the equations of motion for the dual-rotor part are derived by using the finite element method. The finite element discretization of the LP and HP rotors is illustrated in Fig. 3, in which the two rotating shafts are divided into several segments. The rigid discs are arranged on the corresponding nodes according to the actual installation location.
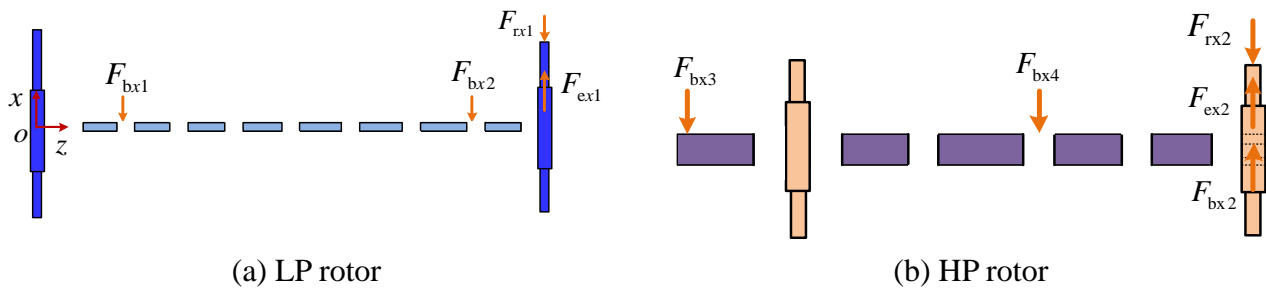
(a) LP rotor   (b) HP rotor

Fig. 3 Finite element discretization of the dual-rotor part in the coordinate plane of *xoz*: (a) LP rotor and (b) HP rotor.

The variable $F_{bxi}(i=1\sim4)$ denotes the vertical component of the constraint force provided by the rolling bearing. F_{bx2} is seen as a particular constraint force provided by the inter-shaft bearing. The variable $F_{rxj}(j=1,2)$ denotes the vertical component of the rub-impact force between the multi-stage turbine blades and the multi-layer casings. In addition, the variable $F_{exj}(j=1,2)$ denotes the vertical component of the imbalance force.

As shown in Figs. 4(a) and (b), Rayleigh beam elements are used to model the shaft segments of the LP and HP rotors. Each Rayleigh beam element has four degrees of freedom at each node, including two translations and two rotations. Therefore, the generalized displacement vector of the shaft element of the LP rotor in the coordinate planes of *xoz* and *yoz* can be expressed as
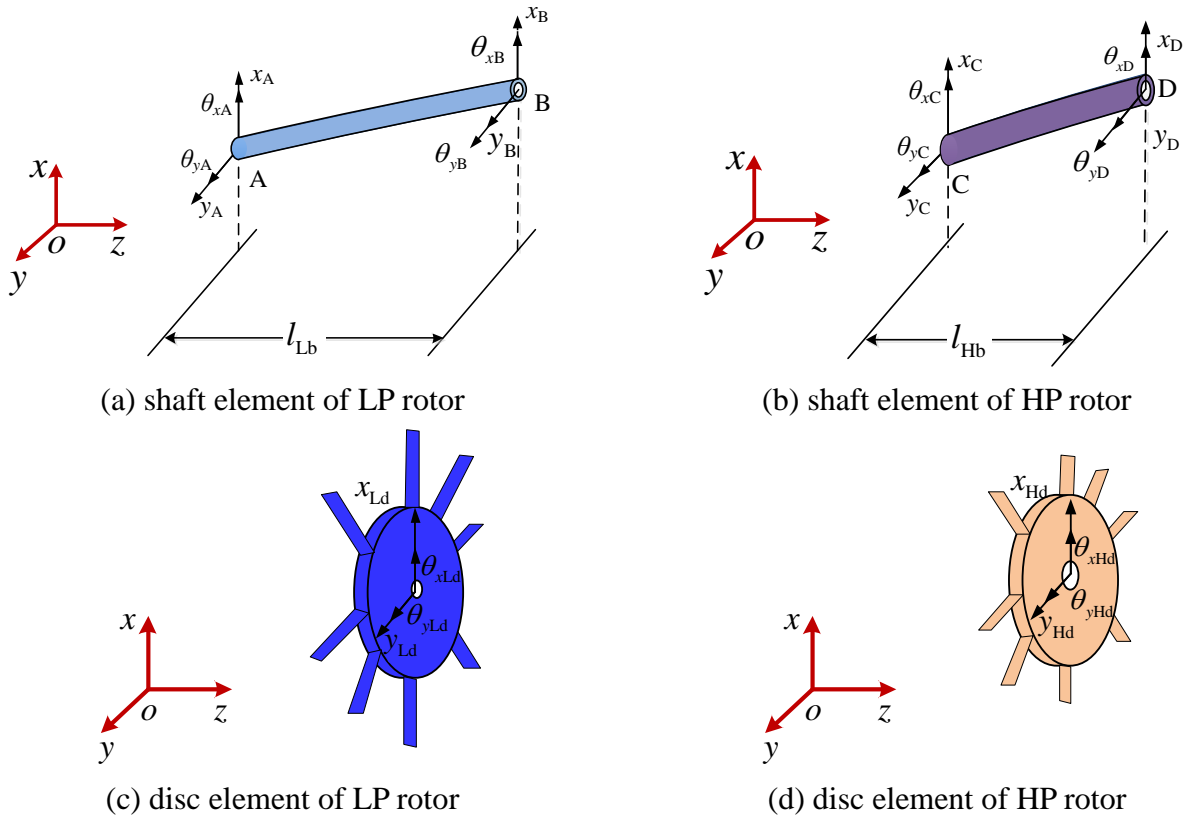
$$\mathbf{u}_{Lb} = \left[x_A, \theta_{yA}, x_B, \theta_{yB}, y_A, -\theta_{xA}, y_B, -\theta_{xB} \right]^T, \tag{1}$$

where x_i and y_i ($i = A, B$) denote the four translations; θ_{xi} and θ_{yi} ($i = A, B$) denote the four rotations, respectively.

Analogously, the generalized displacement vector of the shaft element of the HP rotor can be given as

$$\mathbf{u}_{Hb} = \left[x_C, \theta_{yC}, x_D, \theta_{yD}, y_C, -\theta_{xC}, y_D, -\theta_{xD} \right]^T, \tag{2}$$

where x_i and y_i ($i = C, D$) denote the four translations, θ_{xi} and θ_{yi} ($i = C, D$) denote the four rotations, respectively.

(a) shaft element of LP rotor   (b) shaft element of HP rotor

(c) disc element of LP rotor   (d) disc element of HP rotor

Fig. 4 Discrete elements during the process of the finite element modelling: (a) shaft element of LP rotor, (b) shaft element of HP rotor, (c) disc element of LP rotor, and (d) disc element of HP rotor.

Because of the assumption that all the discs are seen as the rigid ones, the generalized displacement vectors of the discs of the LP and HP rotors (see Figs. 4(c) and (d)) are satisfied as

$$\mathbf{u}_{Ld} = \left[x_{Ld}, \theta_{yLd}, y_{Ld}, -\theta_{xLd} \right]^T, \tag{3}$$

$$\mathbf{u}_{Hd} = \left[x_{Hd}, \theta_{yHd}, y_{Hd}, -\theta_{xHd} \right]^T. \tag{4}$$

As given in [13, 14], the mass matrix of the shaft element usually includes the translational inertia part and the rotational inertia part. In the coordinate plane of *xoz*, the mass matrix of the shaft element of the LP rotor is

$$
\mathbf{M}_{\mathrm{Lb}} = \frac{m_{\mathrm{Lb}}l_{\mathrm{Lb}}}{420}
\begin{bmatrix}
156 & 22l_{\mathrm{Lb}} & 54 & -13l_{\mathrm{Lb}} \\
22l_{\mathrm{Lb}} & 4l_{\mathrm{Lb}}^2 & 13l_{\mathrm{Lb}} & -3l_{\mathrm{Lb}}^2 \\
54 & 13l_{\mathrm{Lb}} & 156 & -22l_{\mathrm{Lb}} \\
-13l_{\mathrm{Lb}} & -3l_{\mathrm{Lb}}^2 & -22l_{\mathrm{Lb}} & 4l_{\mathrm{Lb}}^2
\end{bmatrix}
+ \frac{m_{\mathrm{Lb}}\left(R_{\mathrm{Lb}}^2 + r_{\mathrm{Lb}}^2\right)}{120l_{\mathrm{Lb}}}
\begin{bmatrix}
36 & 3l_{\mathrm{Lb}} & -36 & 3l_{\mathrm{Lb}} \\
3l_{\mathrm{Lb}} & 4l_{\mathrm{Lb}}^2 & -3l_{\mathrm{Lb}} & -l_{\mathrm{Lb}}^2 \\
-36 & -3l_{\mathrm{Lb}} & 36 & -3l_{\mathrm{Lb}} \\
3l_{\mathrm{Lb}} & -l_{\mathrm{Lb}}^2 & -3l_{\mathrm{Lb}} & 4l_{\mathrm{Lb}}^2
\end{bmatrix}, \quad (5)
$$

where m_{Lb} denotes the mass per unit length of the shaft; l_{Lb} denotes the length of the shaft element of the LP rotor; R_{Lb} and r_{Lb} denote the outer and inner radii of the cross section, respectively.

Through the same derivation, the following expression is used to describe the mass matrix of the shaft element of the HP rotor.

$$
\mathbf{M}_{\mathrm{Hb}} = \frac{m_{\mathrm{Hb}}l_{\mathrm{Hb}}}{420}
\begin{bmatrix}
156 & 22l_{\mathrm{Hb}} & 54 & -13l_{\mathrm{Hb}} \\
22l_{\mathrm{Hb}} & 4l_{\mathrm{Hb}}^2 & 13l_{\mathrm{Hb}} & -3l_{\mathrm{Hb}}^2 \\
54 & 13l_{\mathrm{Hb}} & 156 & -22l_{\mathrm{Hb}} \\
-13l_{\mathrm{Hb}} & -3l_{\mathrm{Hb}}^2 & -22l_{\mathrm{Hb}} & 4l_{\mathrm{Hb}}^2
\end{bmatrix}
+ \frac{m_{\mathrm{Hb}}\left(R_{\mathrm{Hb}}^2 + r_{\mathrm{Hb}}^2\right)}{120l_{\mathrm{Hb}}}
\begin{bmatrix}
36 & 3l_{\mathrm{Hb}} & -36 & 3l_{\mathrm{Hb}} \\
3l_{\mathrm{Hb}} & 4l_{\mathrm{Hb}}^2 & -3l_{\mathrm{Hb}} & -l_{\mathrm{Hb}}^2 \\
-36 & -3l_{\mathrm{Hb}} & 36 & -3l_{\mathrm{Hb}} \\
3l_{\mathrm{Hb}} & -l_{\mathrm{Hb}}^2 & -3l_{\mathrm{Hb}} & 4l_{\mathrm{Hb}}^2
\end{bmatrix}, \quad (6)
$$

where m_{Hb} denotes the mass per unit length; l_{Hb} denotes the length of the shaft element of the HP rotor; R_{Hb} and r_{Hb} denote the outer and inner radii of the cross section, respectively.

Under the two imbalance excitations, the whirling motion will appear in the dual-rotor system. In this condition, the polar inertial moments of the two rotating shafts can lead to the gyroscopic effects, which should be taken into consideration.

The gyroscopic matrices of the shaft elements of the LP and HP rotors are given in the following expressions:

$$
\mathbf{G}_{\mathrm{Lb}} = \frac{m_{\mathrm{Lb}}\left(R_{\mathrm{Lb}}^2 + r_{\mathrm{Lb}}^2\right)\omega_{\mathrm{L}}}{60l_{\mathrm{Lb}}}
\begin{bmatrix}
36 & 3l_{\mathrm{Lb}} & -36 & 3l_{\mathrm{Lb}} \\
3l_{\mathrm{Lb}} & 4l_{\mathrm{Lb}}^2 & -3l_{\mathrm{Lb}} & -l_{\mathrm{Lb}}^2 \\
-36 & -3l_{\mathrm{Lb}} & 36 & -3l_{\mathrm{Lb}} \\
3l_{\mathrm{Lb}} & -l_{\mathrm{Lb}}^2 & -3l_{\mathrm{Lb}} & 4l_{\mathrm{Lb}}^2
\end{bmatrix}, \quad (7)
$$

$$
\mathbf{G}_{\mathrm{Hb}} = \frac{m_{\mathrm{Hb}}\left(R_{\mathrm{Hb}}^2 + r_{\mathrm{Hb}}^2\right)\omega_{\mathrm{H}}}{60l_{\mathrm{Hb}}}
\begin{bmatrix}
36 & 3l_{\mathrm{Hb}} & -36 & 3l_{\mathrm{Hb}} \\
3l_{\mathrm{Hb}} & 4l_{\mathrm{Hb}}^2 & -3l_{\mathrm{Hb}} & -l_{\mathrm{Hb}}^2 \\
-36 & -3l_{\mathrm{Hb}} & 36 & -3l_{\mathrm{Hb}} \\
3l_{\mathrm{Hb}} & -l_{\mathrm{Hb}}^2 & -3l_{\mathrm{Hb}} & 4l_{\mathrm{Hb}}^2
\end{bmatrix}, \quad (8)
$$

where ω_{L} and ω_{H} denotes the rotational speeds of the LP and HP rotors.

In addition, the stiffness matrix of the shaft element of the LP rotor in the coordinate plane of *xoz* can be expressed as

$$\mathbf{K}_{\mathrm{Lb}} = \frac{EI_{\mathrm{Lb}}}{l_{\mathrm{Lb}}^3} \begin{bmatrix} 12 & 6l_{\mathrm{Lb}} & -12 & 6l_{\mathrm{Lb}} \\ 6l_{\mathrm{Lb}} & 4l_{\mathrm{Lb}}^2 & -6l_{\mathrm{Lb}} & 2l_{\mathrm{Lb}}^2 \\ -12 & -6l_{\mathrm{Lb}} & 12 & -6l_{\mathrm{Lb}} \\ 6l_{\mathrm{Lb}} & 2l_{\mathrm{Lb}}^2 & -6l_{\mathrm{Lb}} & 4l_{\mathrm{Lb}}^2 \end{bmatrix}, \tag{9}$$

where E denotes the elastic modulus of the LP shaft, I_{Lb} denotes the second moment of area of the cross section of the LP shaft.

Since the LP rotor and the HP rotor have the same material characteristics, the elastic modulus of the HP rotor is also defined as E. Therefore, the stiffness matrix of the shaft element of the HP rotor can be expressed as

$$\mathbf{K}_{\mathrm{Hb}} = \frac{EI_{\mathrm{Hb}}}{l_{\mathrm{Hb}}^3} \begin{bmatrix} 12 & 6l_{\mathrm{Hb}} & -12 & 6l_{\mathrm{Hb}} \\ 6l_{\mathrm{Hb}} & 4l_{\mathrm{Hb}}^2 & -6l_{\mathrm{Hb}} & 2l_{\mathrm{Hb}}^2 \\ -12 & -6l_{\mathrm{Hb}} & 12 & -6l_{\mathrm{Hb}} \\ 6l_{\mathrm{Hb}} & 2l_{\mathrm{Hb}}^2 & -6l_{\mathrm{Hb}} & 4l_{\mathrm{Hb}}^2 \end{bmatrix}, \tag{10}$$

where I_{Hb} denotes the second moment of area of the cross section of the HP shaft.

It must be noted that each disc element has only on node. The mass matrix and the gyroscopic matrix of the disc are written in a 2×2 form in the coordinate plane of *xoz*, namely

$$\begin{cases} \mathbf{M}_{\mathrm{Ld}} = \begin{bmatrix} m_{\mathrm{Ld}} & 0 \\ 0 & J_{\mathrm{Ldd}} \end{bmatrix}, \\ \mathbf{M}_{\mathrm{Hd}} = \begin{bmatrix} m_{\mathrm{Hd}} & 0 \\ 0 & J_{\mathrm{Hdd}} \end{bmatrix}, \end{cases} \tag{11}$$

and

$$\begin{cases} \mathbf{G}_{\mathrm{Ld}} = \omega_{\mathrm{L}} \begin{bmatrix} 0 & 0 \\ 0 & J_{\mathrm{Ldp}} \end{bmatrix}, \\ \mathbf{G}_{\mathrm{Hd}} = \omega_{\mathrm{H}} \begin{bmatrix} 0 & 0 \\ 0 & J_{\mathrm{Hdp}} \end{bmatrix}, \end{cases} \tag{12}$$

where m_{Ld} and m_{Hd} are the mass matrices of the discs of the LP and HP rotors; J_{Ldd} and J_{Hdd} are the diametric inertia of the discs; J_{Ldp} and J_{Hdp} are the polar inertia of the discs, respectively.

Then the equations of motion for the dual-rotor part of the complete system can be obtained by assembling the mass and stiffness matrices of the disc elements and the shaft elements, so that

$$\begin{bmatrix} \mathbf{M}_L & 0 & 0 & 0 \\ 0 & \mathbf{M}_H & 0 & 0 \\ 0 & 0 & \mathbf{M}_L & 0 \\ 0 & 0 & 0 & \mathbf{M}_H \end{bmatrix}\begin{bmatrix} \ddot{\mathbf{u}}_{xL} \\ \ddot{\mathbf{u}}_{xH} \\ \ddot{\mathbf{u}}_{yL} \\ \ddot{\mathbf{u}}_{yH} \end{bmatrix} + \begin{bmatrix} 0 & 0 & \mathbf{G}_L & 0 \\ 0 & 0 & 0 & \mathbf{G}_H \\ -\mathbf{G}_L & 0 & 0 & 0 \\ 0 & -\mathbf{G}_H & 0 & 0 \end{bmatrix}\begin{bmatrix} \dot{\mathbf{u}}_{xL} \\ \dot{\mathbf{u}}_{xH} \\ \dot{\mathbf{u}}_{yL} \\ \dot{\mathbf{u}}_{yH} \end{bmatrix} +$$

$$\begin{bmatrix} \mathbf{K}_L & 0 & 0 & 0 \\ 0 & \mathbf{K}_H & 0 & 0 \\ 0 & 0 & \mathbf{K}_L & 0 \\ 0 & 0 & 0 & \mathbf{K}_H \end{bmatrix}\begin{bmatrix} \mathbf{u}_{xL} \\ \mathbf{u}_{xH} \\ \mathbf{u}_{yL} \\ \mathbf{u}_{yH} \end{bmatrix} = \begin{bmatrix} \mathbf{Q}_{xL} \\ \mathbf{Q}_{xH} \\ \mathbf{Q}_{yL} \\ \mathbf{Q}_{yH} \end{bmatrix}, \tag{13}$$

in which, $\mathbf{M}_L$ and $\mathbf{M}_H$ are the masses matrices of the LP and HP rotor subsystems; $\mathbf{G}_L$ and $\mathbf{G}_H$ are the gyroscopic matrices; $\mathbf{K}_L$ and $\mathbf{K}_H$ are the stiffness matrices; $\mathbf{Q}_{xL}$ and $\mathbf{Q}_{yL}$ are the generalized force vectors acting on the LP rotor; $\mathbf{Q}_{xH}$ and $\mathbf{Q}_{yH}$ are the generalized force vectors acting on the HP rotor, respectively.

It needs to be stressed that the LP rotor and the HP rotor are coupled by the inter-shaft bearing. And the corresponding constraint force between them is reflected in the generalized force vectors of Eq. (13).

2.2 Bearing and pedestal model

As shown in Fig. 2, the dual-rotor part is supported by the rolling bearings and the pedestals. Next the dynamic equations of the rolling bearings and the pedestals are derived in this subsection.

Fig. 5 gives the physical model and the mathematical model of the bearing and the pedestal, which are installed on the LP rotor. According to the motion characteristics, the generalized displacement vector of them is defined as

$$\mathbf{v}_b = \begin{bmatrix} x_{br}, x_p, y_{br}, y_p \end{bmatrix}^T, \tag{14}$$

where x_{br} and x_p denote the vertical displacement of bearing outer ring and pedestal; y_{br} and y_p denote the lateral displacement of bearing outer ring and pedestal, respectively.

(a) physical model   (b) mathematical model
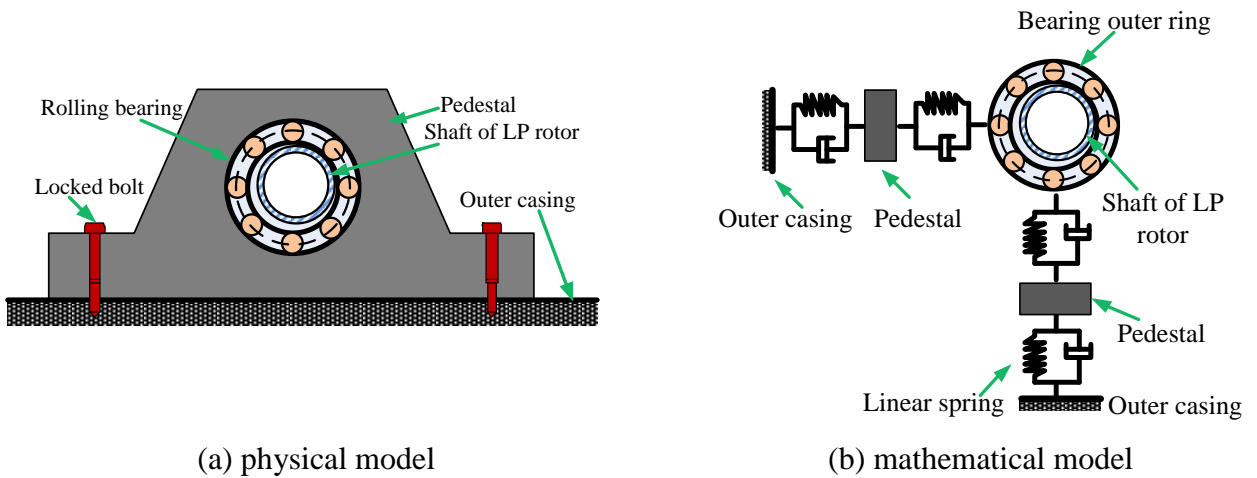
Fig. 5 Schematic diagram of bearing and pedestal models without looseness fault: (a) physical model and (b) mathematical model.

Because the pedestal is connected with the outer casing (see Fig. 5(b)), the interaction between them should be accounted for in the modelling process. Based on the Lagrange's equation, the equations of motion for the bearing outer ring and the pedestal are determined as

$$
\begin{bmatrix} m_{br} & 0 & 0 & 0 \\ 0 & m_p & 0 & 0 \\ 0 & 0 & m_{br} & 0 \\ 0 & 0 & 0 & m_p \end{bmatrix} \begin{bmatrix} \ddot{x}_{br} \\ \ddot{x}_p \\ \ddot{y}_{br} \\ \ddot{y}_p \end{bmatrix} + \begin{bmatrix} c_{br} & -c_{br} & 0 & 0 \\ -c_{br} & c_{br}+c_p & 0 & 0 \\ 0 & 0 & c_{br} & -c_{br} \\ 0 & 0 & -c_{br} & c_{br}+c_p \end{bmatrix} \begin{bmatrix} \dot{x}_{br} \\ \dot{x}_p \\ \dot{y}_{br} \\ \dot{y}_p \end{bmatrix}
$$
$$
+ \begin{bmatrix} k_{br} & -k_{br} & 0 & 0 \\ -k_{br} & k_{br}+k_p & 0 & 0 \\ 0 & 0 & k_{br} & -k_{br} \\ 0 & 0 & -k_{br} & k_{br}+k_p \end{bmatrix} \begin{bmatrix} x_{br} \\ x_p \\ y_{br} \\ y_p \end{bmatrix} = \begin{bmatrix} F_{bx} \\ k_p x_{oc} \\ F_{by} \\ k_p y_{oc} \end{bmatrix},
$$

(15)

where m_{br} and m_p denote the masses of bearing outer ring and pedestal; k_{br} and c_{br} denote the linear stiffness and damping of bearing outer ring; k_p and c_p denote the linear stiffness and damping of pedestal; x_{oc} and y_{oc} denote the vertical and lateral displacement of outer casing.

The above analysis strategy can also be applied to the other bearing and pedestal models. So the equations of motion for all the bearing and pedestal models are presented in this paper.

The specific derivation of forces F_{bx} and F_{by} provided by the rolling balls is further given. Fig. 6 shows two kinds of bearing models, namely support bearing and inter-shaft bearing. Both are mainly composed of inner ring, outer ring and rolling balls. As shown in Fig. 6(a), this bearing is used to support the LP shaft, in which the inner ring of the bearing is in contact with the shaft, and the outer ring is mounted on the pedestal. Different from a support bearing, the inter-shaft bearing (see Fig. 6(b)) is used to realize the coupling relationship between the LP rotor and the HP rotor, where the inner ring of the bearing is in contact with the LP shaft, and the outer ring of the bearing is in contact with the HP shaft.

(a) support bearing   (b) inter-shaft bearing
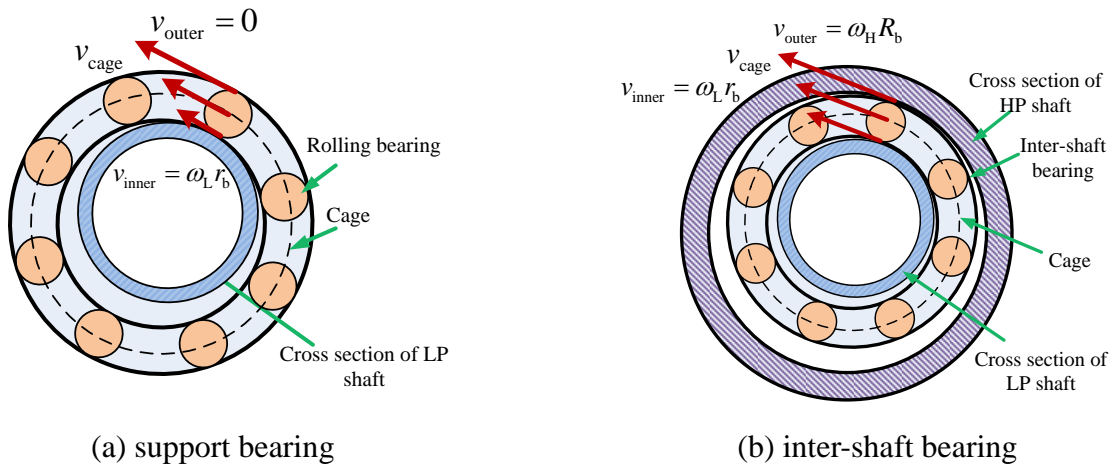
Fig. 6 Schematic diagram of two kinds of bearing models: (a) support bearing and (b) inter-shaft bearing.

According to [37], the cage of the bearing model has no mass but could be considered a geometric constraint that keeps the rolling balls evenly distributed on the circumference. For the

dual-rotor system, there may be four cases for calculating the rotational speed of the cage. Case 1 is the support bearing of the LP rotor; Case 2 is the support bearing of the HP rotor; Case 3 is the inter-shaft bearing under the co-rotation; Case 4 is the inter-shaft bearing under the counter-rotation.

Based on the above four cases the rotational speed of the cage is obtained as

$$
\omega_{\text{cage}} = \frac{v_{\text{outer}} + v_{\text{inner}}}{R_{\text{b}} + r_{\text{b}}} = \begin{cases} \dfrac{\omega_{\text{L}} r_{\text{b}}}{R_{\text{b}} + r_{\text{b}}} & (\text{Case 1}), \\[2mm] \dfrac{\omega_{\text{H}} r_{\text{b}}}{R_{\text{b}} + r_{\text{b}}} & (\text{Case 2}), \\[2mm] \dfrac{\omega_{\text{H}} R_{\text{b}} + \omega_{\text{L}} r_{\text{b}}}{R_{\text{b}} + r_{\text{b}}} & (\text{Case 3}), \\[2mm] \dfrac{\omega_{\text{H}} R_{\text{b}} - \omega_{\text{L}} r_{\text{b}}}{R_{\text{b}} + r_{\text{b}}} & (\text{Case 4}), \end{cases}
\tag{16}
$$

where R_{b} and r_{b} denote the radii of the bearing outer and inner orbits.

For the support bearing shown in Fig. 6(a), the contact displacement of the jth rolling ball satisfies the following expression:

$$
w_j = \left(x_{\text{Lb}} - x_{\text{br}} \right) \sin\left(\omega_{\text{cage}} \times t + \frac{2\pi}{N_{\text{r}}} (j-1) \right) + \left(y_{\text{Lb}} - y_{\text{br}} \right) \cos\left(\omega_{\text{cage}} \times t + \frac{2\pi}{N_{\text{r}}} (j-1) \right) - r_0,
\tag{17}
$$

where x_{Lb} and y_{Lb} are the vertical and lateral displacements of the shaft node corresponding to the installation position of bearing; N_{r} is the number of rolling balls; r_0 is the initial clearance.

If the above contact displacement of the jth rolling ball is larger than zero, the shaft is considered to be subjected to a force from this rolling ball. Otherwise, there is no interaction between them. Therefore, according to the Hertz contact theory [38], the two components of the contact force of the jth rolling ball in the vertical and lateral directions are as follows:

$$
F_{\text{bx}}(j) = \begin{cases} C_{\text{b}} w_j^{\frac{3}{2}} \sin\left(\omega_{\text{cage}} t + \frac{2\pi}{N_{\text{r}}} (j-1) \right) & w_j > 0, \\[2mm] 0 & w_j \leq 0, \end{cases}
\tag{18}
$$

and

$$
F_{\text{by}}(j) = \begin{cases} C_{\text{b}} w_j^{\frac{3}{2}} \cos\left(\omega_{\text{cage}} t + \frac{2\pi}{N_{\text{r}}} (j-1) \right) & w_j > 0, \\[2mm] 0 & w_j \leq 0, \end{cases}
\tag{19}
$$

where C_{b} denotes the contact stiffness of the rolling ball, which is mainly determined by the contact geometry and material characteristics.

By including all the forces from the individual balls, the interaction between the bearing and the LP shaft is obtained as

$$\begin{cases} F_{bx} = \displaystyle\sum_{j=1}^{N_r} F_{bx}(j), \\ F_{by} = \displaystyle\sum_{j=1}^{N_r} F_{by}(j). \end{cases} \tag{20}$$

A schematic diagram of bearing and pedestal models having looseness fault is shown in Fig. 7(a). According to [39], the stiffness and damping forces with tri-linear form are adopted in a nonlinear mathematical model (see Fig. 7(b)).

Hence, the following equations describing the constraint stiffness are acquired:

$$k_p = \begin{cases} k_{p2} & x_p > \delta_1, \\ k_{p1} & 0 \le x_p \le \delta_1, \\ k_{p2} & x_p < 0, \end{cases} \tag{21}$$

where x_p denotes the vertical vibration displacement of the loose pedestal; δ_1 denotes the initial looseness gap; k_{p1} denotes the constraint stiffness under the loose state; k_{p2} denotes the constraint stiffness under the locked state.

Meanwhile, the constraint damping of the pedestal with looseness fault is as follows:

$$c_p = \begin{cases} c_{p2} & y_p > \delta_1, \\ c_{p1} & 0 \le y_p \le \delta_1, \\ c_{p2} & y_p < 0, \end{cases} \tag{22}$$

where c_{p1} denotes the constraint damping under the loose state; c_{p2} denotes the constraint damping under the locked state.

(a) physical model   (b) mathematical model
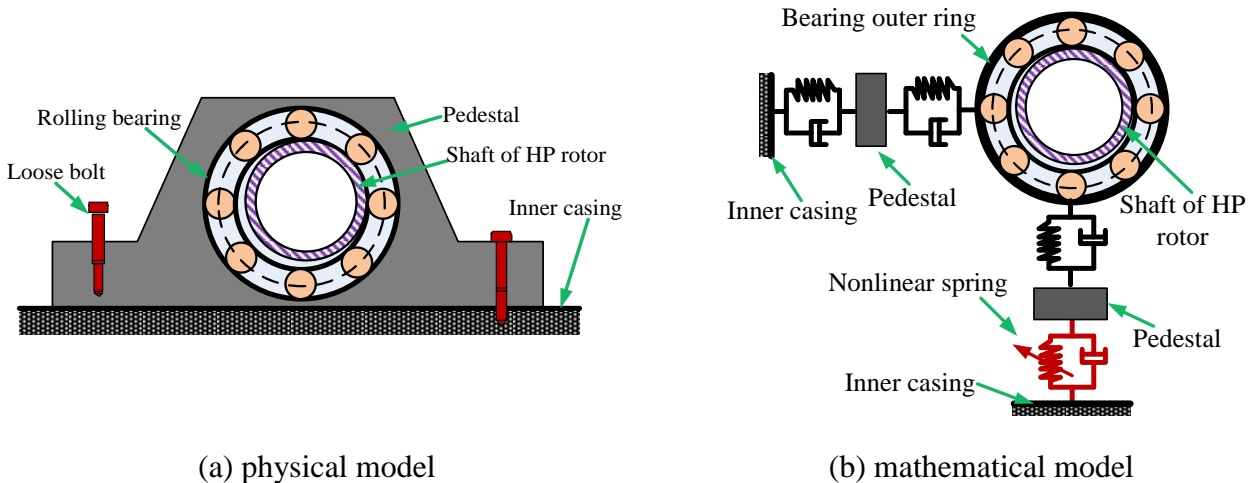
Fig. 7 Schematic diagram of bearing and pedestal models with looseness fault: (a) physical model and (b) mathematical model.

2.3 Inner and outer casing model

For the dual-rotor system established in this paper, the structural stiffness of the inner and outer casings is much greater than that of the flexible shaft. Therefore, the elastic deformations of both inner casing and outer casing are ignored, that is to say, both are modelled as two lumped mass

blocks.

A partial sketch for describing the vibration of inner and outer casings is shown in Fig. 8, in which $F_{\text{p}xi}\,(i=1\sim3)$ denotes the vertical force from three pedestals, and $F_{\text{r}xi}\,(i=1,2)$ denotes the vertical components of rub-impact force. Because of the double casing structure, the multi-stage turbine blades may collide with the inner and outer casings. The mechanical mechanism of rub-impact will be further discussed later.
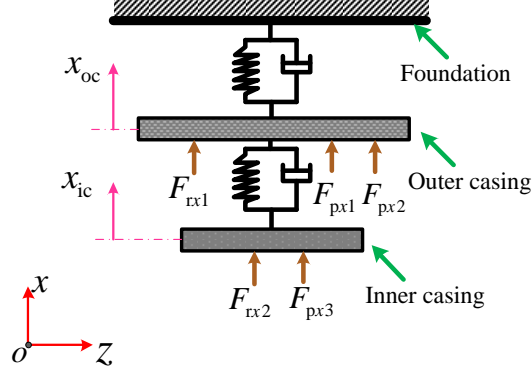
Fig. 8 A partial sketch of inner and outer casings in the coordinate plane of *xoz*.

Through the force analysis for the subsystem shown in Fig. 8, the equations of motion for the inner and outer casings are expressed as

$$\begin{bmatrix} m_{\text{ic}} & 0 & 0 & 0 \\ 0 & m_{\text{oc}} & 0 & 0 \\ 0 & 0 & m_{\text{ic}} & 0 \\ 0 & 0 & 0 & m_{\text{oc}} \end{bmatrix}\begin{bmatrix} \ddot{x}_{\text{ic}} \\ \ddot{x}_{\text{oc}} \\ \ddot{y}_{\text{ic}} \\ \ddot{y}_{\text{oc}} \end{bmatrix} + \begin{bmatrix} c_{\text{ic}} & -c_{\text{ic}} & 0 & 0 \\ -c_{\text{ic}} & c_{\text{ic}}+c_{\text{oc}} & 0 & 0 \\ 0 & 0 & c_{\text{ic}} & -c_{\text{ic}} \\ 0 & 0 & -c_{\text{ic}} & c_{\text{ic}}+c_{\text{oc}} \end{bmatrix}\begin{bmatrix} \dot{x}_{\text{ic}} \\ \dot{x}_{\text{oc}} \\ \dot{y}_{\text{ic}} \\ \dot{y}_{\text{oc}} \end{bmatrix}$$
$$+ \begin{bmatrix} k_{\text{ic}} & -k_{\text{ic}} & 0 & 0 \\ -k_{\text{ic}} & k_{\text{ic}}+k_{\text{oc}} & 0 & 0 \\ 0 & 0 & k_{\text{ic}} & -k_{\text{ic}} \\ 0 & 0 & -k_{\text{ic}} & k_{\text{ic}}+k_{\text{oc}} \end{bmatrix}\begin{bmatrix} x_{\text{ic}} \\ x_{\text{oc}} \\ y_{\text{ic}} \\ y_{\text{oc}} \end{bmatrix} = \begin{bmatrix} F_{\text{r}x2} \\ F_{\text{r}x1} \\ F_{\text{r}y2} \\ F_{\text{r}y1} \end{bmatrix} + \begin{bmatrix} F_{\text{p}x3} \\ F_{\text{p}x1}+F_{\text{p}x2} \\ F_{\text{p}y3} \\ F_{\text{p}y1}+F_{\text{p}y2} \end{bmatrix}, \tag{23}$$

where m_{ic} and m_{oc} represent the masses of inner and outer casings; k_{oc} and k_{ic} represent the constraint stiffness; c_{oc} and c_{ic} represent the constraint damping, respectively.

2.4 Multi-stage turbine blade-casing rub model

Due to two imbalance excitations and pedestal looseness, serious rub-impact fault between the multi-stage turbine blades and the multi-layer casings may be induced. Consequently, the mechanical mechanism of blade-casing rub is revealed in this subsection.

Usually, soft coating is used for the low pressure rotor, while hard coating is used for the high pressure rotor. Then the influences of coatings painted on the aero-engine components are considered in this paper. As shown in Fig. 9, the LP turbine disc with blades may rub against the outer casing with soft coating. Meanwhile, the HP turbine disc with blades may also rub against the inner casing with hard coating. It is assumed that N_{L} and N_{H} blades are evenly distributed on the two turbine discs. So the angular positions of the *i*th blade of the LP turbine disc and the *j*th blade of the HP turbine disc at time t can be determined as

$$\begin{cases} \phi_{Lb}(i) = \dfrac{2\pi}{N_L}(i-1) + \omega_L t, \\ \phi_{Hb}(j) = \dfrac{2\pi}{N_H}(j-1) + \omega_H t. \end{cases} \tag{24}$$

On the basis of Eq. (24), the impact displacement and the impact velocity between the ith blade and the outer casing can be further obtained as

$$\begin{cases} \delta_L(i) = (y_{Ld} - y_{oc})\cos(\phi_{Lb}(i)) + (x_{Ld} - x_{oc})\sin(\phi_{Lb}(i)) - \delta_{L0}, \\ \dot{\delta}_L(i) = (\dot{y}_{Ld} - \dot{y}_{oc})\cos(\phi_{Lb}(i)) + (\dot{x}_{Ld} - \dot{x}_{oc})\sin(\phi_{Lb}(i)), \end{cases} \tag{25}$$

where δ_{L0} denotes the initial gap between the blades of LP turbine disc and the outer casing.

In the same way, the impact displacement and the impact velocity between the jth blade of the HP turbine disc and the inner casing are

$$\begin{cases} \delta_H(j) = (y_{Hd} - y_{ic})\cos(\phi_{Hb}(j)) + (x_{Hd} - x_{ic})\sin(\phi_{Hb}(j)) - \delta_{H0}, \\ \dot{\delta}_H(j) = (\dot{y}_{Hd} - \dot{y}_{ic})\cos(\phi_{Hb}(j)) + (\dot{x}_{Hd} - \dot{x}_{ic})\sin(\phi_{Hb}(j)), \end{cases} \tag{26}$$

where δ_{H0} denotes the initial gap between the blades of HP turbine disc and the inner casing.

(a) LP turbine disc and outer casing with soft coating

(b) HP turbine disc and inner casing with hard coating
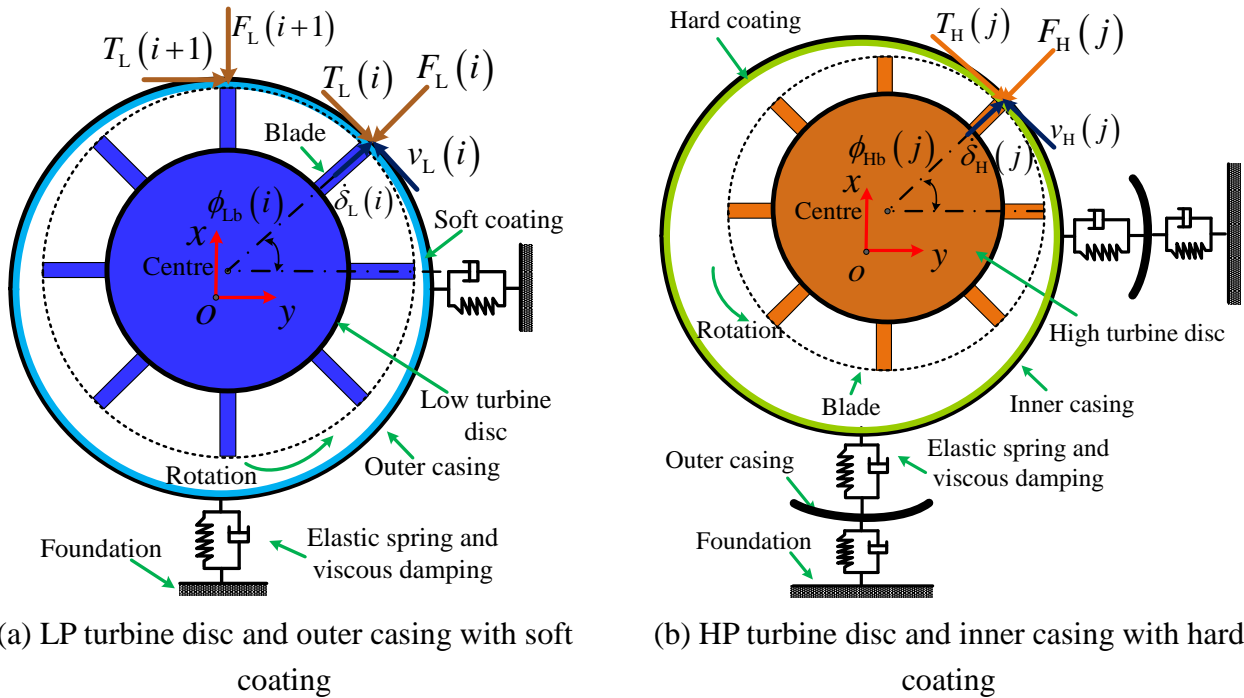
Fig. 9 Schematic diagram of rub-impact between multi-stage turbine blades and multi-layer casings: (a) LP turbine disc and outer casing with soft coating and (b) HP turbine disc and inner casing with hard coating.

Then the Lankarani-Nikravesh model [40] is utilized to describe the mechanical mechanism of rub-impact between multi-stage turbine blades and multi-layer casings. This contact model is developed from the Hertz contact theory and accounts for several features, such as local contact area, material characteristics and energy loss.

As a result, the impact forces of the ith blade of the LP turbine disc and the jth blade of the HP

turbine disc are obtained as

$$F_{\mathrm{L}}(i) = \begin{cases} k_{\mathrm{L}}\left(\delta_{\mathrm{L}}(i)\right)^{\frac{3}{2}}\left(1 + \dfrac{3\left(1-c_e^2\right)\dot{\delta}_{\mathrm{L}}(i)}{4\dot{\delta}_{\mathrm{L}}^{-}(i)}\right) & \delta_{\mathrm{L}}(i) \geq 0, \\ 0 & \delta_{\mathrm{L}}(i) < 0, \end{cases} \tag{27}$$

and

$$F_{\mathrm{H}}(j) = \begin{cases} k_{\mathrm{H}}\left(\delta_{\mathrm{H}}(j)\right)^{\frac{3}{2}}\left(1 + \dfrac{3\left(1-c_e^2\right)\dot{\delta}_{\mathrm{H}}(j)}{4\dot{\delta}_{\mathrm{H}}^{-}(j)}\right) & \delta_{\mathrm{H}}(j) \geq 0, \\ 0 & \delta_{\mathrm{H}}(j) < 0, \end{cases} \tag{28}$$

where k_{L} and k_{H} denote the impact stiffness, which is mainly determined by the elastic modulus of coatings and the curvature radius in the contact area. In the numerical simulation, two values are used to describe the two different impact stiffness caused by the different coating hardness. Moreover, c_e denotes the restitution coefficient; $\dot{\delta}_{\mathrm{L}}^{-}(i)$ and $\dot{\delta}_{\mathrm{H}}^{-}(j)$ denote the initial impact velocity, respectively.

The tangential rub between the blades and the casings is seen as a sliding friction in this paper. Accordingly, the Coulomb friction law [41] is employed as

$$\begin{cases} T_{\mathrm{L}}(i) = \mu_{\mathrm{L}}\,\mathrm{sgn}\left(v_{\mathrm{L}}(i)\right)F_{\mathrm{L}}(i), \\ T_{\mathrm{H}}(j) = \mu_{\mathrm{H}}\,\mathrm{sgn}\left(v_{\mathrm{H}}(j)\right)F_{\mathrm{H}}(i), \end{cases} \tag{29}$$

where μ_{L} and μ_{H} denote the coefficients of friction, which are mainly determined by the smoothness of soft and hard coatings.

Fig. 9 suggests that the sign function in Eq. (29) depends primarily on the tangential relative velocity between the two surfaces at the blade-casing contact points. Therefore, the tangential relative velocities $v_{\mathrm{L}}(i)$ and $v_{\mathrm{H}}(j)$ can be determined as

$$\begin{cases} v_{\mathrm{L}}(i) = \omega_{\mathrm{L}}\left(R_{\mathrm{Ld}} + l_{\mathrm{Lb}}(i)\right) + \left(\dot{x}_{\mathrm{Ld}} - \dot{x}_{\mathrm{oc}}\right)\cos\left(\phi_{\mathrm{Lb}}(i)\right) - \left(\dot{y}_{\mathrm{Ld}} - \dot{y}_{\mathrm{oc}}\right)\sin\left(\phi_{\mathrm{Lb}}(i)\right), \\ v_{\mathrm{H}}(j) = \omega_{\mathrm{H}}\left(R_{\mathrm{Hd}} + l_{\mathrm{Hb}}(j)\right) + \left(\dot{x}_{\mathrm{Hd}} - \dot{x}_{\mathrm{ic}}\right)\cos\left(\phi_{\mathrm{Hb}}(j)\right) - \left(\dot{y}_{\mathrm{Hd}} - \dot{y}_{\mathrm{ic}}\right)\sin\left(\phi_{\mathrm{Hb}}(j)\right), \end{cases} \tag{30}$$

where R_{Ld} and R_{Hd} denote the outer radii of the turbine discs; $l_{\mathrm{Lb}}(i)$ and $l_{\mathrm{Hb}}(j)$ denote the length of the ith blade and the jth blade, respectively.

The total rub-impact force of the dual-rotor system is the sum of the rub-impact forces acting on the blades of the turbine discs. So the impact forces and the tangential forces could be further transformed as the external forces in Eq. (23) by using the following relations:

$$\begin{cases} F_{\mathrm{rx1}} = \displaystyle\sum_{i=1}^{N_{\mathrm{L}}}\left(-F_{\mathrm{L}}(i)\sin\left(\phi_{\mathrm{Lb}}(i)\right) - T_{\mathrm{L}}(i)\cos\left(\phi_{\mathrm{Lb}}(i)\right)\right), \\ F_{\mathrm{ry1}} = \displaystyle\sum_{i=1}^{N_{\mathrm{L}}}\left(-F_{\mathrm{L}}(i)\cos\left(\phi_{\mathrm{Lb}}(i)\right) + T_{\mathrm{L}}(i)\sin\left(\phi_{\mathrm{Lb}}(i)\right)\right), \end{cases} \tag{31}$$

and

$$\begin{cases} F_{rx2} = \sum_{j=1}^{N_H}\left(-F_H(j)\sin\left(\phi_{Hb}(j)\right)-T_H(j)\cos\left(\phi_{Hb}(j)\right)\right), \\ F_{ry2} = \sum_{j=1}^{N_H}\left(-F_H(j)\cos\left(\phi_{Hb}(j)\right)+T_H(j)\sin\left(\phi_{Hb}(j)\right)\right). \end{cases} \tag{32}$$

2.5 Integration of the dual-rotor-bearing-double casing model

Based on the previous analysis, the discrete parts, including dual-rotor part, bearings, pedestals, inner casing and outer casing, are further integrated here. Therefore, the equation of motion for the dual-rotor-bearing-double casing system can be written in the following matrix form.

$$\begin{bmatrix} \mathbf{M}_L & 0 & 0 & 0 & 0 & 0 \\ 0 & \mathbf{M}_H & 0 & 0 & 0 & 0 \\ 0 & 0 & \mathbf{M}_C & 0 & 0 & 0 \\ 0 & 0 & 0 & \mathbf{M}_L & 0 & 0 \\ 0 & 0 & 0 & 0 & \mathbf{M}_H & 0 \\ 0 & 0 & 0 & 0 & 0 & \mathbf{M}_C \end{bmatrix} \begin{bmatrix} \ddot{\mathbf{u}}_{xL} \\ \ddot{\mathbf{u}}_{xH} \\ \ddot{\mathbf{u}}_{xC} \\ \ddot{\mathbf{u}}_{yL} \\ \ddot{\mathbf{u}}_{yH} \\ \ddot{\mathbf{u}}_{yC} \end{bmatrix} + \begin{bmatrix} 0 & 0 & 0 & \mathbf{G}_L & 0 & 0 \\ 0 & 0 & 0 & 0 & \mathbf{G}_H & 0 \\ 0 & 0 & \mathbf{C}_C & 0 & 0 & 0 \\ -\mathbf{G}_L & 0 & 0 & 0 & 0 & 0 \\ 0 & -\mathbf{G}_H & 0 & 0 & 0 & 0 \\ 0 & 0 & 0 & 0 & 0 & \mathbf{C}_C \end{bmatrix} \begin{bmatrix} \ddot{\mathbf{u}}_{xL} \\ \ddot{\mathbf{u}}_{xH} \\ \ddot{\mathbf{u}}_{xC} \\ \ddot{\mathbf{u}}_{yL} \\ \ddot{\mathbf{u}}_{yH} \\ \ddot{\mathbf{u}}_{yC} \end{bmatrix}$$
$$+ \begin{bmatrix} \mathbf{K}_L & 0 & 0 & 0 & 0 & 0 \\ 0 & \mathbf{K}_H & 0 & 0 & 0 & 0 \\ 0 & 0 & \mathbf{K}_C & 0 & 0 & 0 \\ 0 & 0 & 0 & \mathbf{K}_L & 0 & 0 \\ 0 & 0 & 0 & 0 & \mathbf{K}_H & 0 \\ 0 & 0 & 0 & 0 & 0 & \mathbf{K}_C \end{bmatrix} \begin{bmatrix} \mathbf{u}_{xL} \\ \mathbf{u}_{xH} \\ \mathbf{u}_{xC} \\ \mathbf{u}_{yL} \\ \mathbf{u}_{yH} \\ \mathbf{u}_{yC} \end{bmatrix} = \begin{bmatrix} \mathbf{Q}_{xL} \\ \mathbf{Q}_{xH} \\ \mathbf{Q}_{xC} \\ \mathbf{Q}_{yL} \\ \mathbf{Q}_{yH} \\ \mathbf{Q}_{yC} \end{bmatrix}, \tag{33}$$

where $\mathbf{M}_C$, $\mathbf{C}_C$, $\mathbf{K}_C$ denote the mass, damping, stiffness matrices of the subsystem, which includes the bearings, pedestals, inner casing and outer casing. Moreover, $\mathbf{Q}_{xC}$ and $\mathbf{Q}_{yC}$ denote the generalized force vector of this subsystem.

3. Experimental study on the dual-rotor rig

To predict the vibration behaviour of the dual-rotor system subjected to two imbalance excitations, an experimental study at different rotational speeds is performed on a dual-rotor test rig.

(a) external construction   (b) inner construction   (c) blade-casing rub
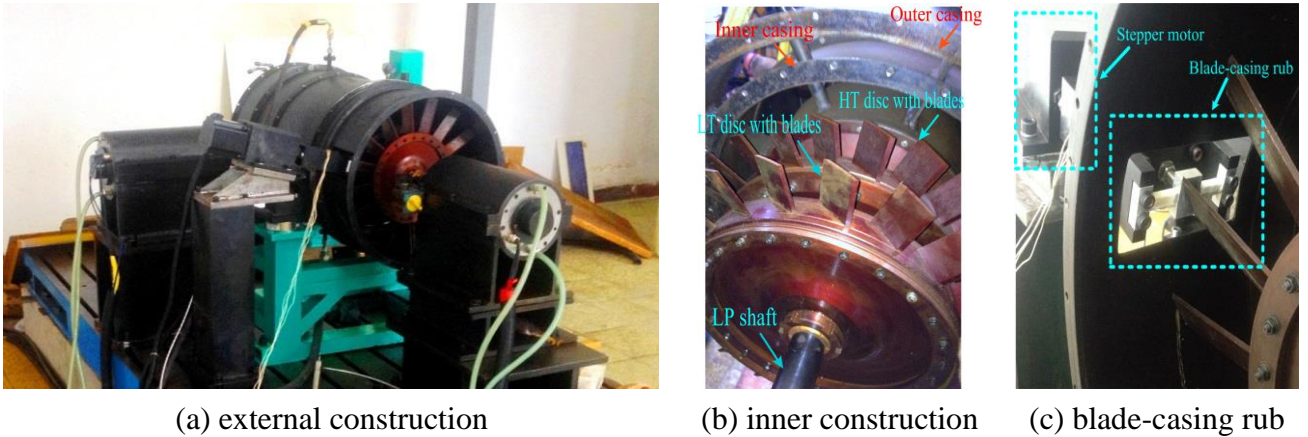
Fig. 10 Diagram of a dual-rotor test rig: (a) external construction, (b) inner construction, and (c)

blade-casing rub.

Fig. 10 shows the dual-rotor test rig, which is set up in the Aircraft Dynamics and Vibration Control Lab, Harbin Institute of Technology. The main structural characteristics of the test rig are very close to the theoretical model proposed in this paper. Both the LP rotor and the HP rotor are driven by their own motors. As shown in Fig. 10(b), a double casing is present and several straight blades are installed on the two turbine discs.

3.1 Effect of speed ratio of LP and HP rotors

This subsection focuses on the vibration features of the dual-rotor test rig with different speed ratios of LP and HP rotors. The speed ratio of the LP and HP rotors is defined as

$$\eta = \frac{\omega_L}{\omega_H}, \tag{34}$$

where $\eta > 0$ indicates the co-rotation state, and $\eta < 0$ indicates the counter-rotation state.

In this paper, co-rotation of the dual-rotor test rig is considered. To understand the dynamic responses more comprehensively, the speed ratio of the LP and HP rotors is set to $\eta \approx 1$, $\eta \approx 1.1$, $\eta = 1.2$ and $\eta = 1.4$, respectively. For the turbine disc of the LP rotor, the time histories of lateral displacement are shown in Fig. 11.
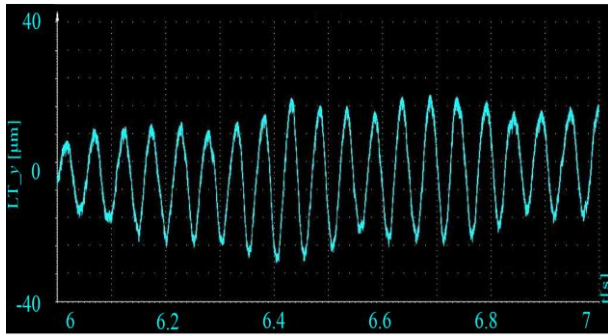
(a) $\omega_L = 190$ rad/s and $\omega_H = 194$ rad/s
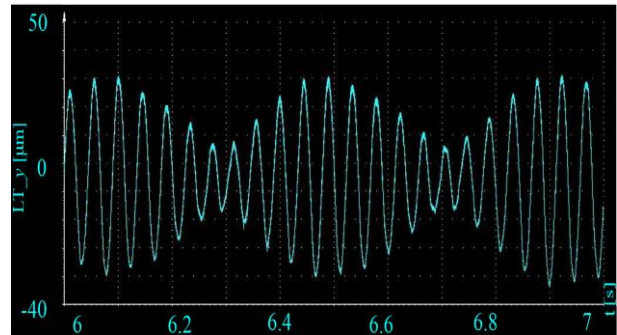
(b) $\omega_L = 195$ rad/s and $\omega_H = 217$ rad/s
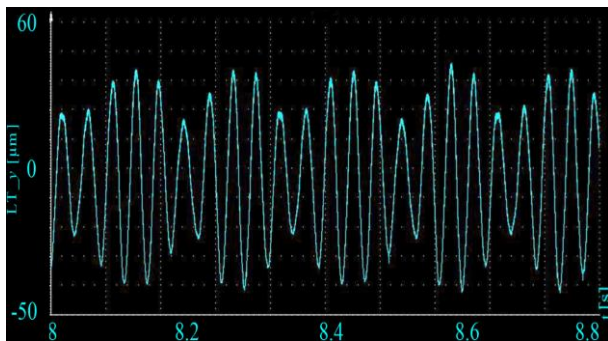
(c) $\omega_L = 200$ rad/s and $\omega_H = 240$ rad/s
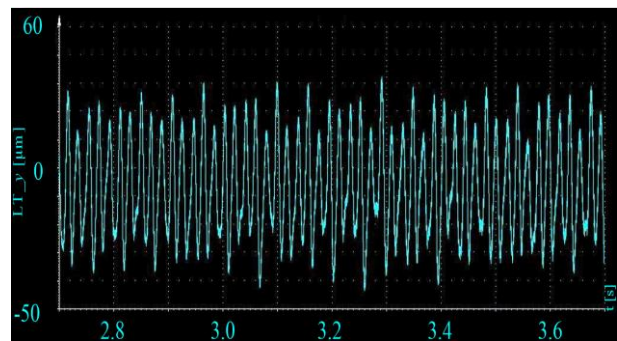
(d) $\omega_L = 350$ rad/s and $\omega_H = 490$ rad/s

Fig. 11 Time histories of lateral displacement in the different condition of speed ratio: (a) $\omega_L = 190$ rad/s and $\omega_H = 194$ rad/s, (b) $\omega_L = 195$ rad/s and $\omega_H = 217$ rad/s, (c) $\omega_L = 200$ rad/s and $\omega_H = 240$ rad/s, (d) $\omega_L = 350$ rad/s and $\omega_H = 490$ rad/s.

From Fig. 11, it is clear that there are different types of vibration behaviours. Fig. 11(a) shows a transition from periodic motion to beat vibration. When the speed ratio is $\eta \approx 1.1$ and $\eta \approx 1.2$, the

time histories of lateral displacement obviously exhibit beat vibration, while the period of beat vibration under $\eta \approx 1.1$ is different from that under $\eta \approx 1.2$. Furthermore, with the increase of speed ratio, the phenomenon of beat vibration will be gradually replaced by quasi-periodic motion, as shown in Fig. 11(d).

Hence it can be concluded that when the rotational speed of the LP rotor is close to that of the HP rotor, the beat vibration is more likely to occur in the dynamic responses of the dual-rotor system.

3.2 Vibration response in simulation and experiment

The experimental study in the previous subsection illustrates that the beat vibration is a typical dynamic behaviour for the dual-rotor system. In view of this, the beat vibration is emphatically investigated by numerical simulation and experiment. Under the excitation, the vibration responses of the system include the transient-state part and the steady-state part. In order to capture the dynamic characteristics of the system, the steady-state part is selected and studied.

In terms of experiment, multiple eddy current sensors are used to simultaneously measure the lateral and vertical displacements of the LP turbine disc. When the rotational speeds of the LP and HP rotors are $\omega_L = 200$ rad/s and $\omega_H = 240$ rad/s, the vibration responses in the two directions are shown in Figs. 12(a) and (b).
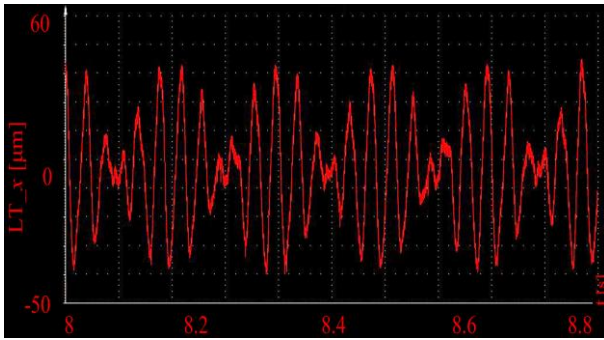
(a) experimental result in vertical direction   (b) experimental result in lateral direction
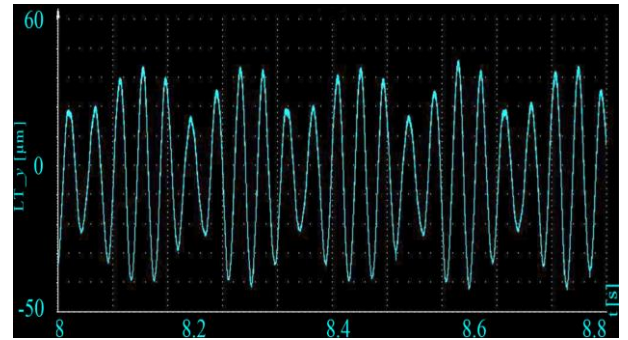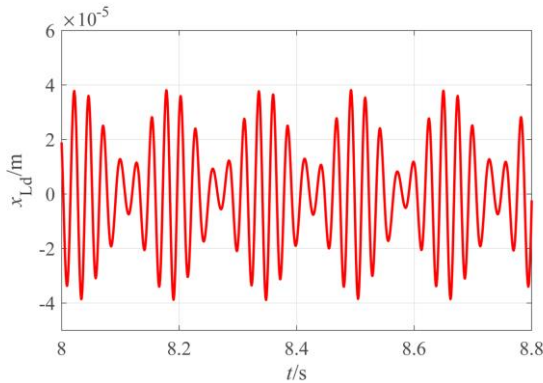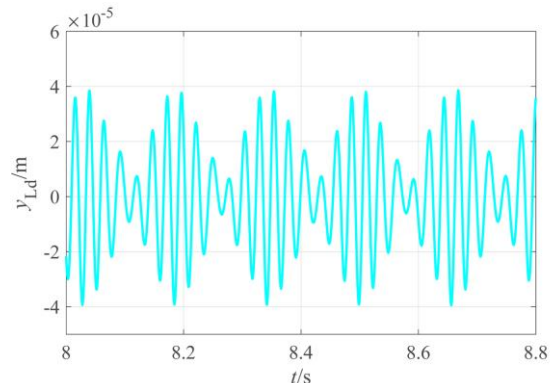
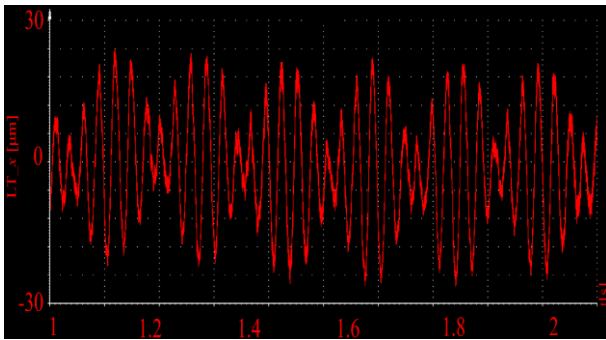(c) theoretical result in vertical direction   (d) theoretical result in lateral direction

Fig. 12 Time histories of displacement of the LP turbine disc at $\omega_L = 200$ rad/s and $\omega_H = 240$ rad/s : (a) experimental result in vertical direction, (b) experimental result in lateral direction, (c) theoretical result in vertical direction, and (d) theoretical result in lateral direction.

The main parameters of the dual-rotor system in the simulation are taken from [13] and given in the Appendix. Then the fourth-order Runge-Kutta method is applied to carry out the dynamics

simulation of Eq. (33). Keeping the rotational speeds of the LP and HP rotors unchanged, the numerical results for describing the vertical and lateral displacements of LP turbine disc are depicted in Figs. 12(c) and (d). By comparative analysis, it can be seen that the numerical results are well matched with the experimental results, including the vibration amplitude and the vibration period. Obviously, there is one beat in every $0.1\,\text{s}$.

While keeping $\eta = 1.2$, the rotational speed of the LP rotor is increased to $\omega_\text{L} = 300\,\text{rad/s}$. Consequently, the displacements of the LP turbine disc obtained by simulation and experiment are given in Fig. 13. It is clear that the phenomenon of beat vibration still exists in the responses of the dual-rotor system. More importantly, the theoretical results are basically consistent with the experimental results.
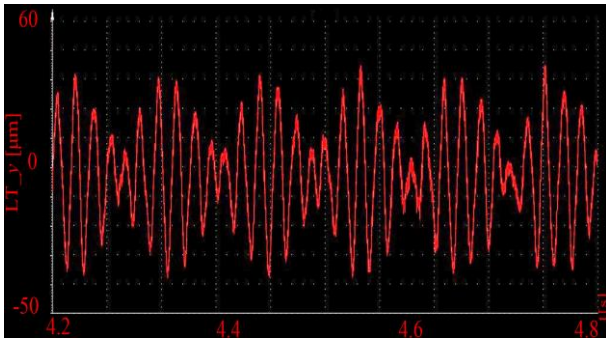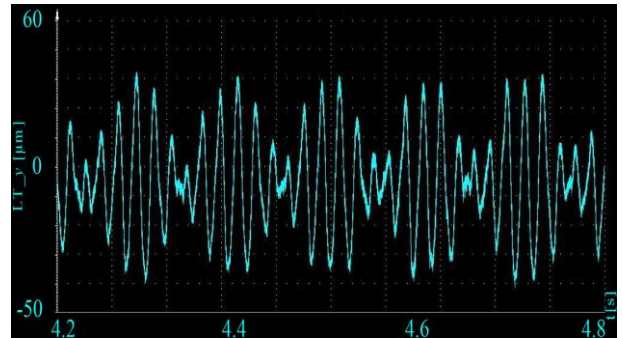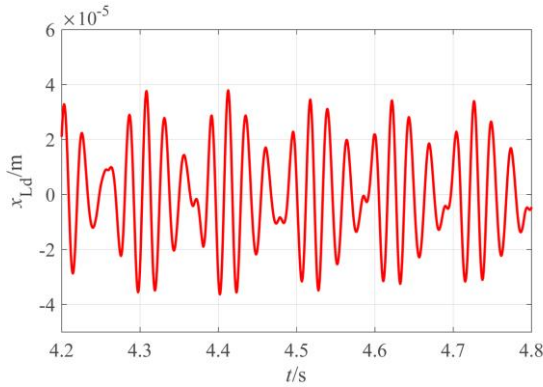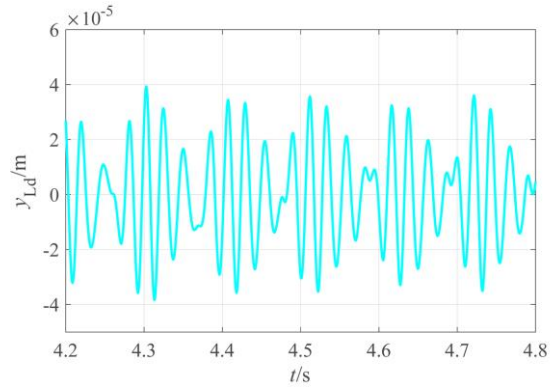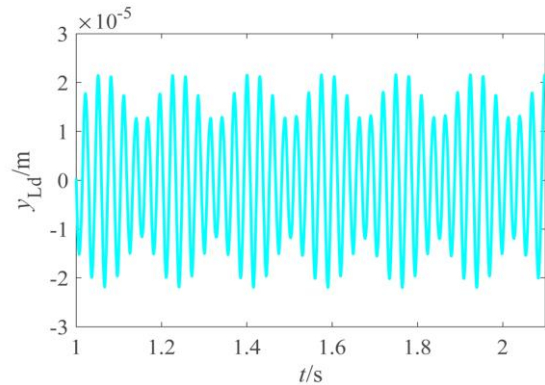

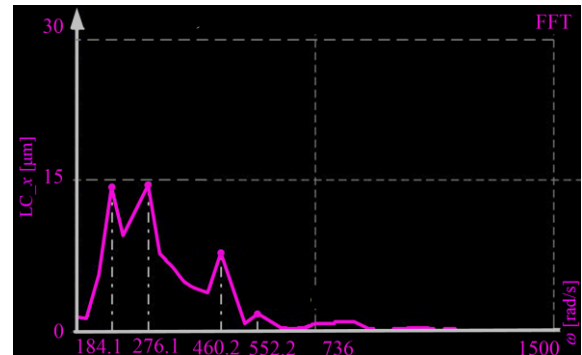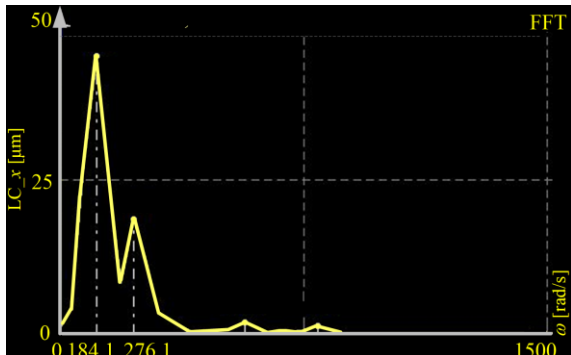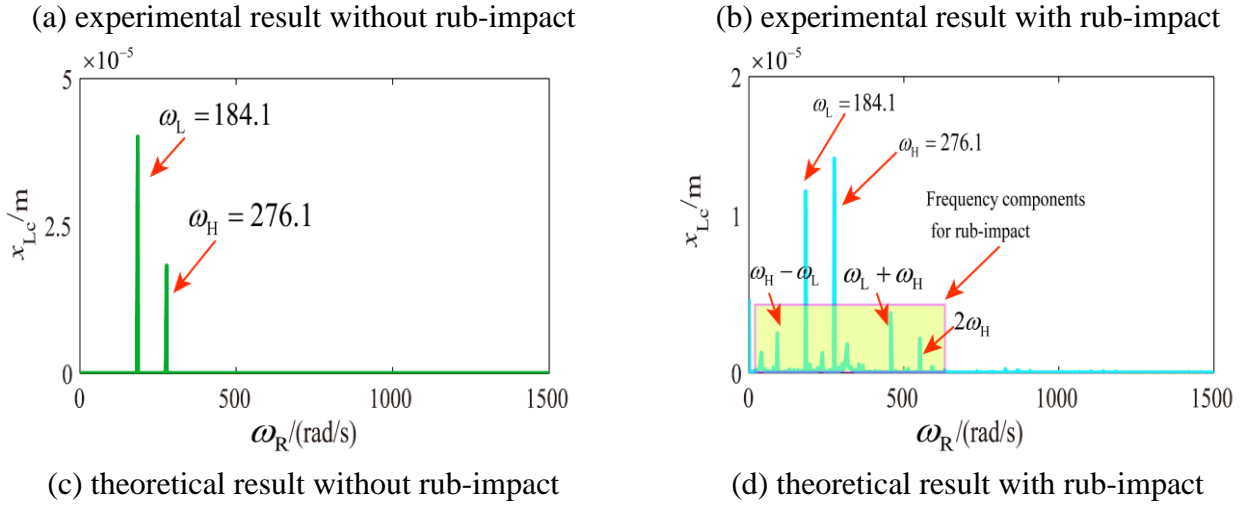| (a) experimental result in vertical direction | (b) experimental result in lateral direction |

| (c) theoretical result in vertical direction | (d) theoretical result in lateral direction |

Fig. 13 Time histories of displacement of the LP turbine disc at $\omega_\text{L} = 300\,\text{rad/s}$ and $\omega_\text{H} = 360\,\text{rad/s}$: (a) experimental result in vertical direction, (b) experimental result in lateral direction, (c) theoretical result in vertical direction, and (d) theoretical result in lateral direction.

For a dual-rotor system, there are generally two operating modes, namely co-rotation and counter-rotation. The so-called co-rotation means that the rotation direction of the HP rotor is the same as that of the LP rotor. However, the so-called counter-rotation means that the rotation direction of the HP rotor is opposite to that of the LP rotor. For the case of co-rotation, the theoretical and experimental research on the beat vibration has been conducted. Next, by theoretical and experimental methods, the vibration response of the dual-rotor system is further studied in the counter-rotation mode.

As shown in Fig. 14, when the rotational speeds of the LP and HP rotors are $\omega_\text{L} = 180\,\text{rad/s}$

and $\omega_H = -216$, the phenomenon of beat vibration is observed in Fig. 14, in which the theoretical result is similar to the experimental result.

Combined with the structural characteristics of the experimental platform, a rub testing device is designed at the low pressure disc (see Fig. 10(c)), and the blade-casing rub experiment is carried out accordingly. As shown in Fig. 15, the frequency spectrum of the system without and with blade-casing rub is respectively obtained by theoretical and experimental methods. When the blade-casing rub is not considered, Figs. 15(a) and (c) only contain two frequency components, i.e., two excitation frequencies of the LP and HP rotors. Due to blade-casing rub, there are rich frequency components in Figs. 15(b) and (d), including ω_L, ω_H, $\omega_H - \omega_L$, $\omega_L + \omega_H$ and $2\omega_H$. In addition, rub response obtained by the theoretical method is consistent with that obtained by the experiment.

(a) experimental result in vertical direction   (b) experimental result in lateral direction
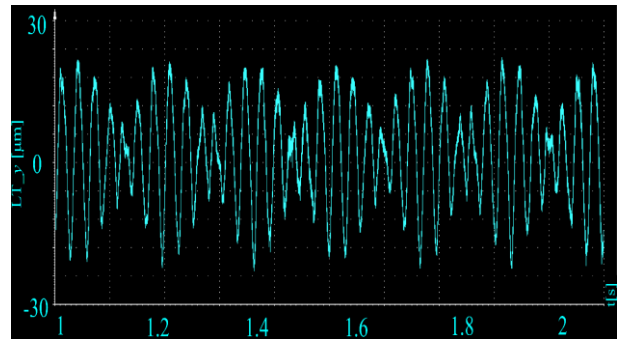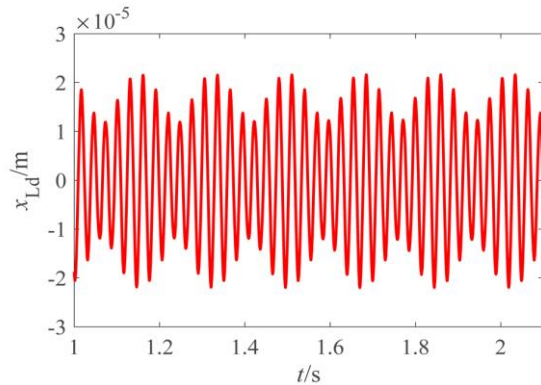
(c) theoretical result in vertical direction   (d) theoretical result in lateral direction

Fig. 14 Time histories of displacement of the LP turbine disc at $\omega_L = 180$ rad/s and $\omega_H = -216$ rad/s: (a) experimental result in vertical direction, (b) experimental result in lateral direction, (c) theoretical result in vertical direction, and (d) theoretical result in lateral direction.

(a) experimental result without rub-impact (b) experimental result with rub-impact

(c) theoretical result without rub-impact (d) theoretical result with rub-impact

Fig. 15 Frequency spectra of the vertical responses of the dual-rotor system at $\omega_{\mathrm{L}} = 184$ rad/s and $\omega_{\mathrm{H}} = 276$ rad/s : (a) experimental result without rub-impact, (b) experimental result with rub-impact, (c) theoretical result without rub-impact, and (d) theoretical result with rub-impact.

In this subsection, the comparison between the theoretical result and the experimental result is carried out. This illustrates that the dynamic model of the dual-rotor-bearing-double casing system proposed in this paper is effective to some extent. Based on this model, the vibration response of the system having pedestal looseness and blade-casing rub will be further investigated by numerical simulation in the following part.

4. Simulation and discussion

4.1 Dynamic analysis of the system with pedestal looseness

In this part, the effects of the pedestal looseness on the vibration responses of the dual-rotor-bearing-double casing system are studied numerically. In the simulation process, a linear interpolation method [42] is adopted to determine the occurrence of the blade-casing rub. For a case of 'no rub to rub', the initial time step is modified by the linear interpolation method. When the target condition is satisfied, the iteration for refining the time step will stop. The parameters given in the Appendix are used in the simulation. Then the time histories, whirling orbits and spectrum cascades are used to describe the dynamic responses of the system in different work conditions.

Keeping the rotational speed of the LP rotor as $\omega_{\mathrm{L}} = 200$ rad/s, the speed ratio is set to $\eta = 1$ and $\eta = 1.2$, respectively. For the case of no looseness, the time histories of the vertical displacements of inner and outer casings are shown in Figs. 16(a) and (b). At $\eta = 1$, the vibration responses of the inner and outer casings are regular 1T-periodic motion. While at $\eta = 1.2$, the responses of the inner and outer casings evolve into beat vibration. Regardless of the above two speed ratios, the vibration amplitude of the inner casing is always larger than that of the outer casing.

Next the pedestal looseness shown in Fig. 7(b) is accounted for and the stiffness of the loosening pedestal given in Eq. (21) is set to $k_{\mathrm{p1}} = 0$, which represents the most serious state. Under this circumstance, the vertical displacements of the inner and outer casings are shown in Figs. 16(c)

and (d). It can be seen that the responses appear in pulses. Because of the decrease of the constraint stiffness caused by pedestal looseness, the vertical vibration amplitudes are obviously amplified. In addition, it should be emphasized that although the looseness fault only occurs in the local part of the HP rotor, both the LP rotor and the HP rotor will vibration violently. The main reason is that the LP rotor and the HP rotor are coupled through the inter-shaft bearing. Similarly, the dynamic responses of the inner casing and the outer casing are linked as well. In addition, according to the change of vibration amplitude shown in Fig. 16, it can be observed that the vibration of the system having pedestal looseness happens around a position which is not zero.

To some extent, these particular dynamic phenomena, such as impulse responses with large amplitude and offset of vibration balance position can be used to determine whether there is a looseness fault in a rotating machine.
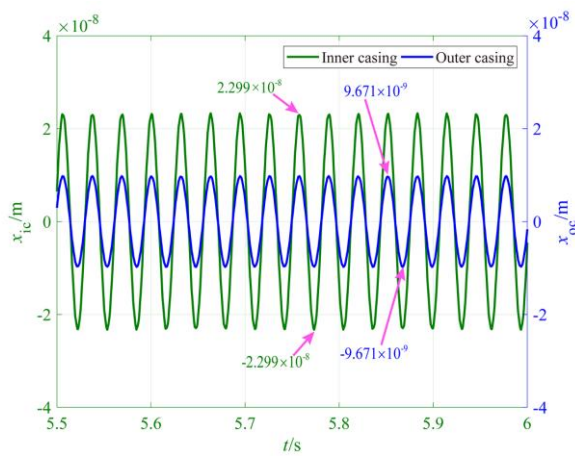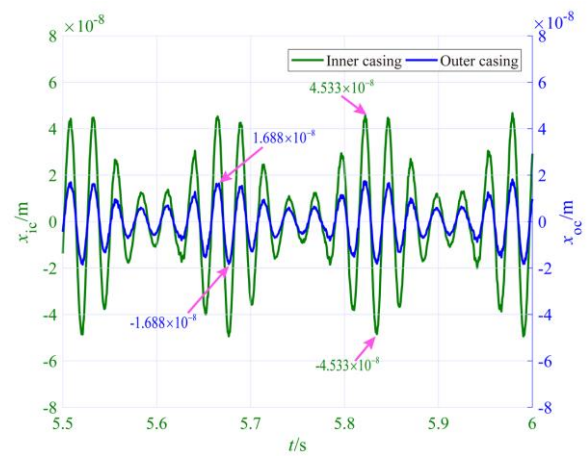
(a) no looseness and $\eta = 1$ (b) no looseness and $\eta = 1.2$
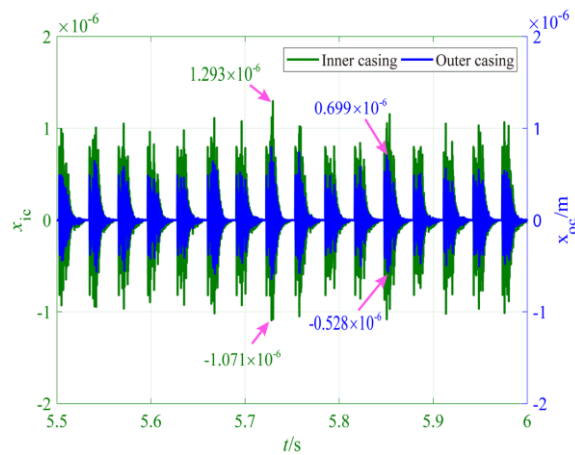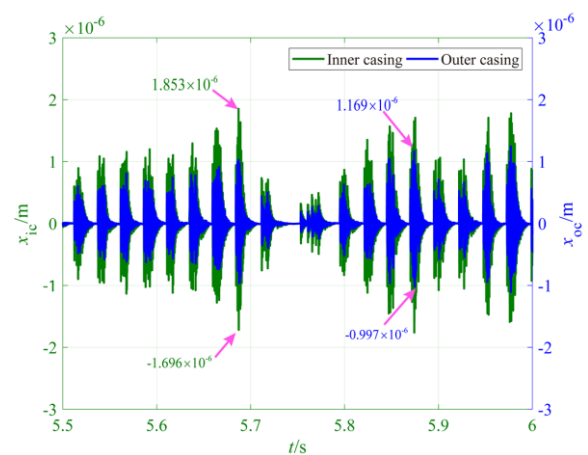
(c) looseness and $\eta = 1$ (d) looseness and $\eta = 1.2$

Fig. 16 Time histories of vertical displacement of the inner and outer casings: (a) with no looseness and $\eta = 1$, (b) with no looseness and $\eta = 1.2$, (c) with looseness and $\eta = 1$, and (d) with looseness and $\eta = 1.2$.

The above simulation proves that the pedestal looseness does have a significant influence on the rotor motion. To understand the motion state of rotating machine clearly, the analysis of whirling orbits is also an indispensable part in the field of rotor dynamics.

Fig. 17 shows the whirling orbits of the inner and outer casings corresponding to the different looseness severity. The state of $\eta = 1$ indicates that the excitation frequency of the LP rotor is equal to that of the HP rotor. In this condition, with the decrease of pedestal stiffness k_{p1}, the whirling orbits of the inner and outer casings gradually change from the initial regular circle to the irregular ellipse. Since the looseness fault mainly exists in the vertical direction, the variations of the whirling orbits in the vertical direction become more obvious than those in the lateral direction.

When the speed ratio is $\eta = 1.2$, the whirling orbits of the inner and outer casings with no looseness appear in a rose-like shape instead of a circle, as shown in Figs. 17(c) and (d). As the looseness severity increases, the rose-like shape disappears, and then it becomes irregular and complicated.
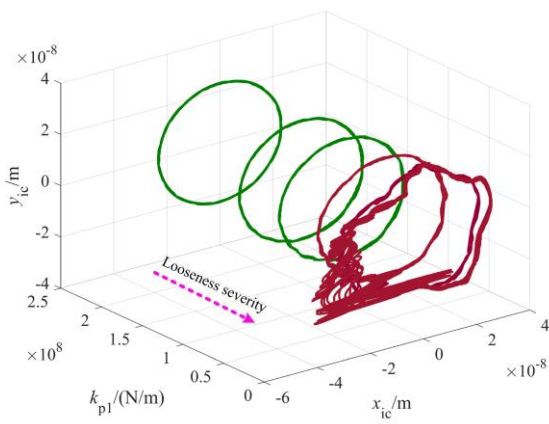
(a) whirling orbits of inner casing at $\eta = 1$ 　　　 (b) whirling orbits of outer casing at $\eta = 1$
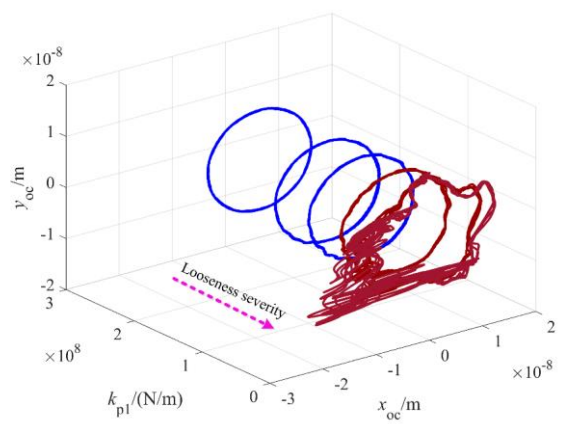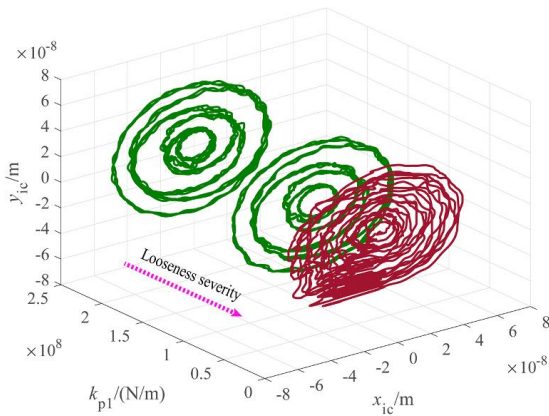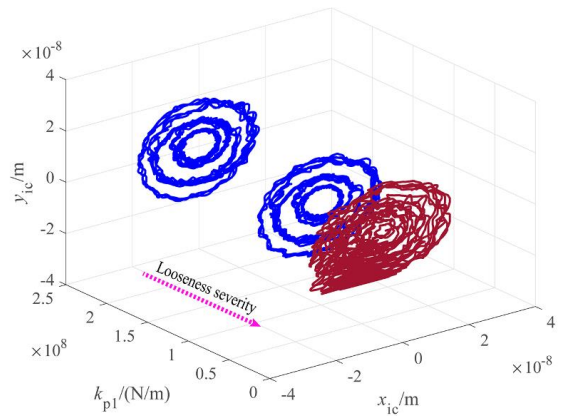
(c) whirling orbits of inner casing at $\eta = 1.2$ 　　 (d) whirling orbits of outer casing at $\eta = 1.2$

Fig. 17 Variation of whirling orbits with different looseness severity: (a) whirling orbits of inner casing at $\eta = 1$, (b) whirling orbits of outer casing at $\eta = 1$, (c) whirling orbits of inner casing at $\eta = 1.2$, and (d) whirling orbits of outer casing at $\eta = 1.2$.

In terms of fault diagnosis, the spectrum feature analysis is an essential tool, which can identify the specific frequency components. Therefore, the 3D waterfall plot is introduced in this part to analyse the frequency characteristics. In order to avoid the complex situation caused by the two

different excitation frequencies, and to more directly analyse the dynamic characteristics corresponding to the looseness fault, the speed ratio of the LP and HP rotors is set to $\eta = 1$ here.

As shown in Fig. 18, the axis of the pedestal stiffness can be divided into two parts, including moderate states and serious states. Under the moderate states, only one frequency component (i.e., excitation frequency) is observed in the 3D waterfall plot. This indicates that the dual-rotor system has not been significantly affected by the pedestal looseness at this time.
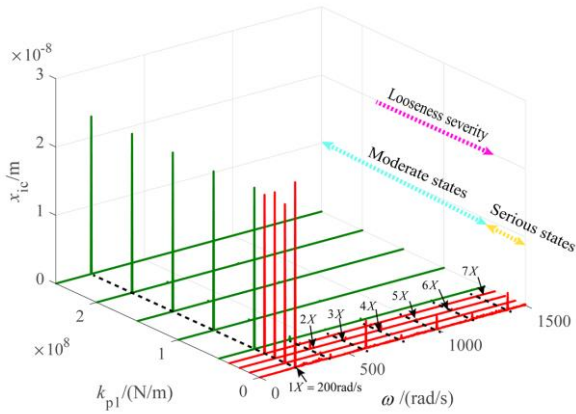
(a) frequency spectrum of vertical displacement of inner casing
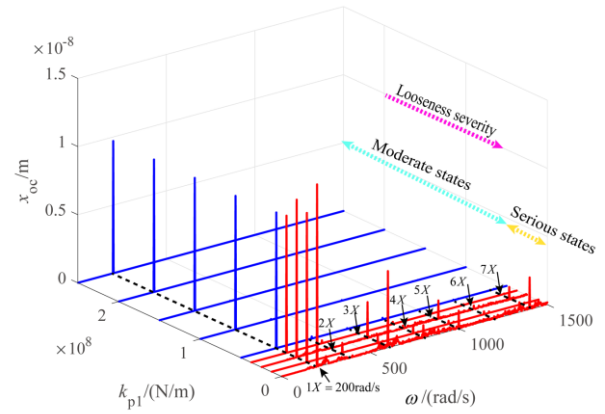
(b) frequency spectrum of vertical displacement of outer casing
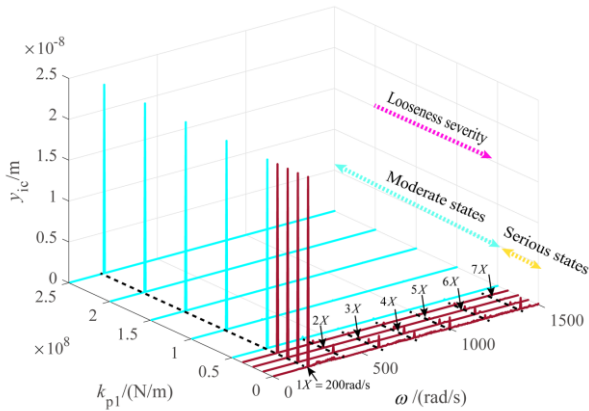
(c) frequency spectrum of lateral displacement of inner casing
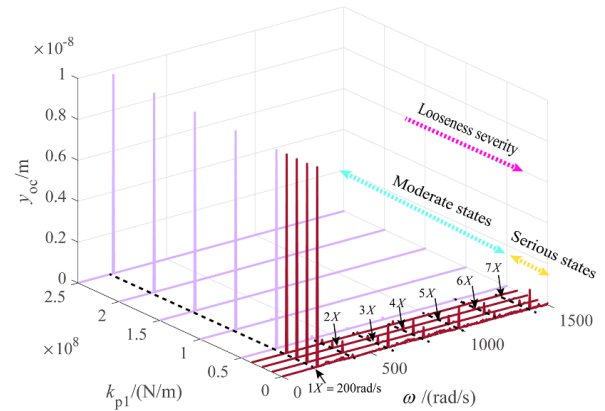
(d) frequency spectrum of lateral displacement of outer casing

Fig. 18 The 3D waterfall plot of the inner and outer casings: (a) frequency spectrum of vertical displacement of inner casing, (b) frequency spectrum of vertical displacement of outer casing, (c) frequency spectrum of lateral displacement of inner casing, and (d) frequency spectrum of lateral displacement of outer casing.

When the pedestal stiffness belongs to the serious states, there are rich frequency components in the 3D waterfall plot. In addition to the component synchronous to rotational speed (i.e., $1X$ component), the higher-order harmonics, such as $2X$, $3X$, $4X$, $5X$, $6X$ and $7X$, are observed in the spectrum diagram. Meanwhile, the amplitude of the $1X$ component is larger than the other components. So it can be concluded that the existence of higher-order harmonics also provides a theoretical basis for the identification of pedestal looseness.

The excitations induced by the mass imbalance are a major source of rotor vibrations. So it is necessary to analyse the effect of disc eccentricities on the motion of the dual-rotor system. Keeping the other parameters unchanged, the eccentricities of the LP turbine disc and the HP turbine disc are assumed to be $e_{Ld} = e_{Hd} = [1,2,3,4,5,6,7,8,9,10] \times 10^{-5}$ mm, respectively.

When the rotational speeds of the LP and HP rotors are $\omega_L = 200$ rad/s and $\omega_H = 240$ rad/s, the variations of the maximum displacements due to different eccentricities are depicted in Fig. 19. Meanwhile, the comparison of the displacement with or without pedestal looseness is also conducted and shown in this figure. With the increase of the disc eccentricities, the maximum vertical displacements gradually become larger. Within this range of disc eccentricities, the looseness fault always aggravates the system vibration. It can enlarge the growth rate of the displacement as well.

The numerical results confirm exactly that the disc eccentricities have a detrimental effect on the smooth operation of rotating machines. In order to prevent the serious amplification of vibration amplitude by looseness fault, more attention should be paid to the effective maintenance of pedestals.
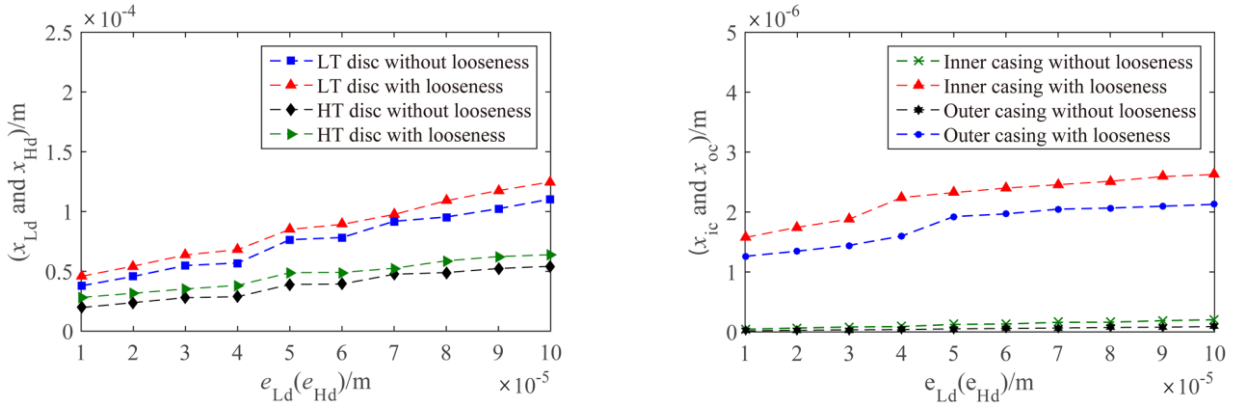
(a) maximum vertical displacement of LP turbine disc (LT disc) and HP turbine disc (HT disc)

(b) maximum vertical displacement of inner and outer casings

Fig. 19 Effects of eccentricities of LT and HT discs on the system responses: (a) maximum vertical displacement of LT and HT discs, and (b) maximum vertical displacement of inner and outer casings.

4.2 Dynamic analysis of the system with looseness-rub coupled fault

The severe imbalance and pedestal looseness can easily lead to the whirling motion with large amplitude. Under this circumstance, the probability of rotor-stator rub is increased sharply. So this subsection concentrates on studying the impact force and fault form of the dual-rotor system.

Different from previous studies [23-25], the rub-impact between multi-stage turbine blades and multi-layer casings is taken as the object. It is worth noting that this is one of the main contributions of this paper. During dual-rotor operation, the blades mounted on the LP turbine disc may rub against the outer casing with soft coating. At the same time, the blades mounted on the HP turbine disc may rub against the inner casing with hard coating as well. Therefore, it is crucial to calculate the impact force between the blades and the casings for evaluating the operation state of the dual-rotor system in advance.

When the effects of the pedestal looseness are not taken into account, the resultant impact forces of the dual-rotor system are analysed at $\eta = 1$ and $\eta = 1.2$. Compared with the HP rotor, the LP

rotor is the first to rub at the rotational speed $\omega_L = 200$ rad/s, as shown in Figs. 20(a) and (b). In the range of LP rotational speed of $[200,375]$rad/s, the LP rotor sustains a full annular rub but there is no contact between the HP rotor and the inner casing. After that, a partial rub replaces the full annular rub and lasts until $\omega_L = 425$ rad/s. Besides, affected by the LP rotor, the HP rotor also begins to rub and the fault form is identified as the partial rub.
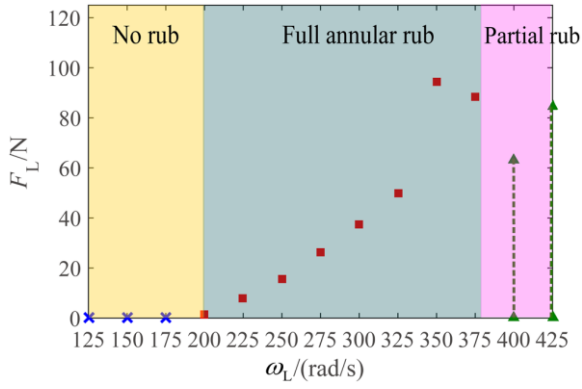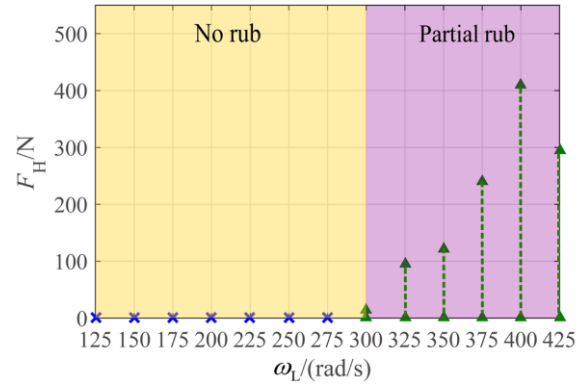

(a) impact force of LP rotor at $\eta = 1$
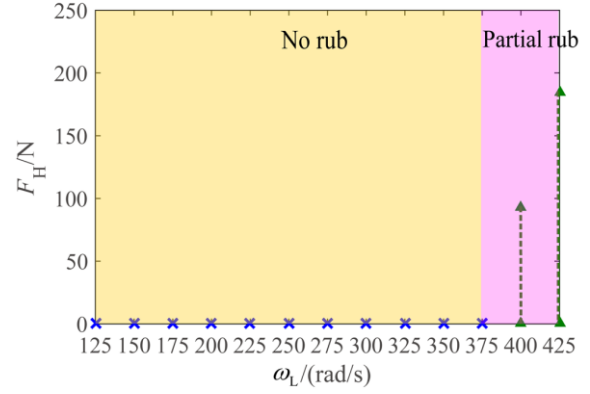
(b) impact force of HP rotor at $\eta = 1$
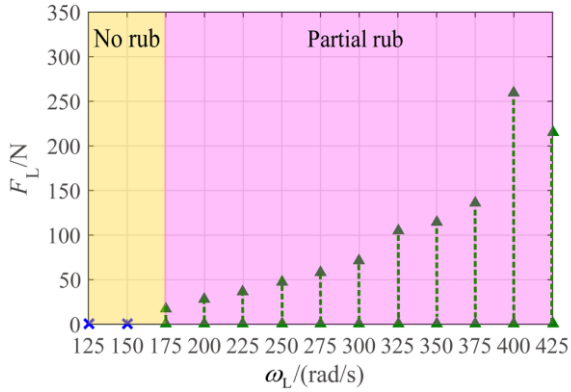
(c) impact force of LP rotor at $\eta = 1.2$

(d) impact force of HP rotor at $\eta = 1.2$

Fig. 20 Resultant impact force of the dual-rotor system without pedestal looseness: (a) impact force of LP rotor at $\eta = 1$, (b) impact force of HP rotor at $\eta = 1$, (c) impact force of LP rotor at $\eta = 1.2$, and (d) impact force of HP rotor at $\eta = 1.2$.

When the speed ratio of the LP and HP rotors is $\eta = 1.2$, the impact forces of the dual-rotor system are given in Figs. 20(c) and (d). Unlike the cases in Figs. 20(a) and (b), the rub-impact of the dual-rotor system happens at a lower speed. Meanwhile, the impact forces in Figs. 20(c) and (d) are larger than those in Figs. 20(a) and (b), which means that the more serious rub-impact happens at this time. From the perspective of fault form, the partial rub is more likely to occur in the dual-rotor system at speed ratio $\eta = 1.2$.

After a preliminary numerical analysis of the rub-impact between the multi-stage turbine blades and the multi-layer casings, the influences of pedestal looseness on the rub characteristics of the dual-rotor system are further discussed in detail.

As shown in Fig. 21(a), the presence of the pedestal looseness will cause the LP rotor to start a

partial rub from $\omega_L = 125$ rad/s. When the rotational speed increases to $\omega_L = 225$ rad/s, a full annular rub happens and lasts until $\omega_L = 375$ rad/s. After this, the full annular rub is replaced by a partial rub again. The variation of the impact force of the HP rotor having pedestal looseness is shown in Fig. 21(b). With the weakening of the constraint stiffness, the HP rotor will rub at a lower rotational speed. Meanwhile, the impact magnitude between the high turbine blades and the inner casing will be intensified by the pedestal looseness.
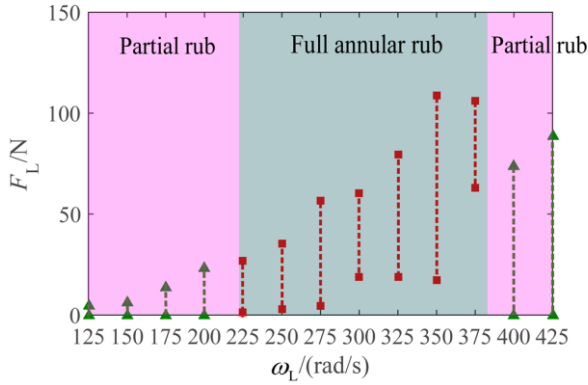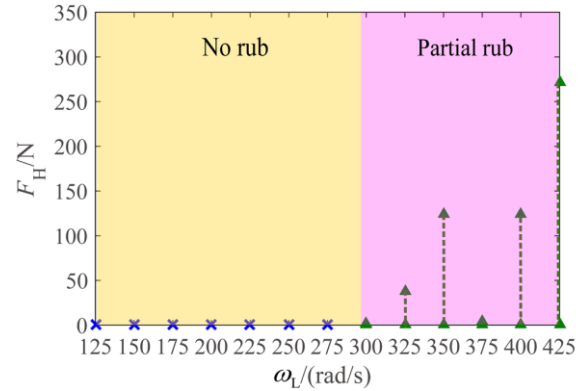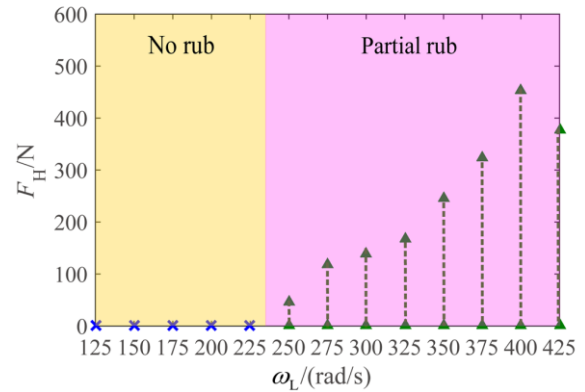

(a) impact force of LP rotor at $\eta = 1$ (b) impact force of HP rotor at $\eta = 1$
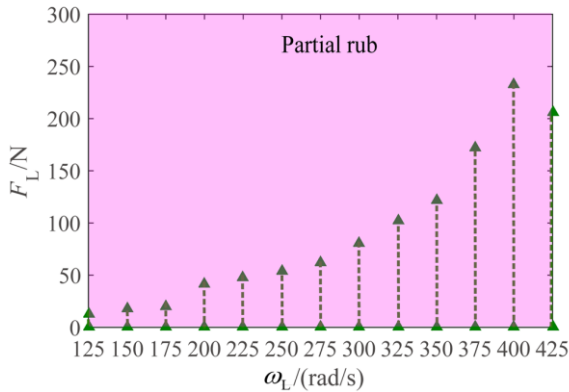
(c) impact force of LP rotor at $\eta = 1.2$ (d) impact force of HP rotor at $\eta = 1.2$

Fig. 21 Resultant impact force of the dual-rotor system having pedestal looseness: (a) impact force of LP rotor at $\eta = 1$, (b) impact force of HP rotor at $\eta = 1$, (c) impact force of LP rotor at $\eta = 1.2$, and (d) impact force of HP rotor at $\eta = 1.2$.

If the speed ratio is changed from $\eta = 1$ to $\eta = 1.2$, the impact forces of the dual-rotor system having pedestal looseness are depicted in Figs. 21(c) and (d). Within the rotational speed range of $[125, 425]$ rad/s, the LP rotor is continuously affected by the partial rub. Meanwhile, compared with Fig. 20(d), the rotational speed corresponding to the first rub will go down even further, as shown in Fig. 21(d).

Finally, the whirling orbits of the LP turbine disc and the HP turbine disc are discussed at different rotational speed ratios. When the rotational speeds of the LP and HP rotors are $\omega_L = 300$ rad/s and $\omega_H = 300$ rad/s, the whirling orbits of the LP turbine disc and the HP turbine
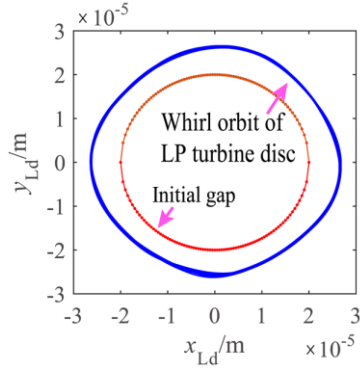
disc exhibit two regular circles, as shown in Figs. 22(a) and (b). Among them, the radius of the former is larger than the initial gap, which indicates the occurrence of full annular rub, while the radius of the latter is less than the initial gap, which indicates that no rub happens.
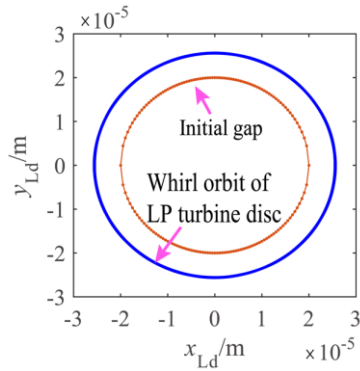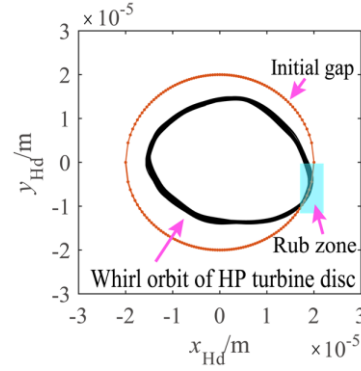

(a) LP rotor without pedestal looseness
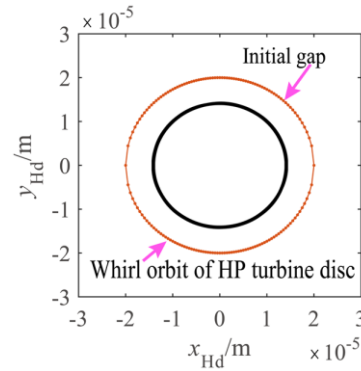
(b) HP rotor without pedestal looseness

(c) LP rotor with pedestal looseness

(d) HP rotor with pedestal looseness

Fig. 22 Whirling orbits of the dual-rotor system at $\omega_L = 300$ rad/s and $\omega_H = 300$ rad/s: (a) LP rotor without pedestal looseness, (b) HP rotor without pedestal looseness, (c) LP rotor with pedestal looseness, and (d) HP rotor with pedestal looseness.

Keeping the other parameters constant, the effects of the pedestal looseness are further considered. Then the corresponding whirling orbits of the system are shown in Figs. 22(c) and (d). Although the whirling orbit is an ellipse, the whirling displacement of the LP turbine disc is always larger than the initial gap. This explains the phenomenon shown in Fig. 21(a) that the LP rotor is subjected to a full annular rub, but the magnitude of rubbing is not constant. Since the whirling displacement of the HP turbine disc is only larger than the initial gap in a limited area, the fault form of the HP rotor is identified as a partial rub.
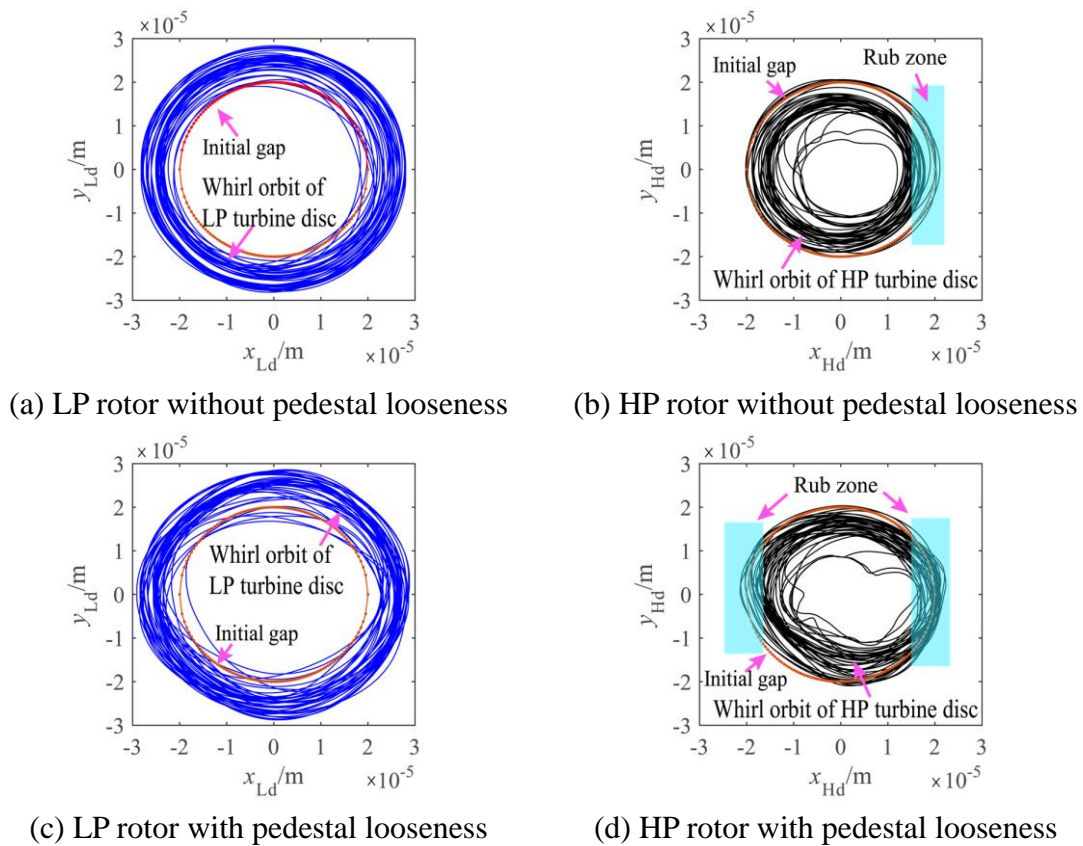
At $\omega_L = 300$ rad/s and $\omega_H = 360$ rad/s, the whirling orbits of the dual-rotor system with and without pedestal looseness are shown in Fig. 23. Due to the pedestal looseness, the whirling orbit is in an ellipse-like shape, which is formed by a large number of dense curves. As the amplitude of whirling motion increases, rub-impact will occur in more areas.

To sum up, the pedestal looseness will obviously induce rub-impact, especially partial rub. Meanwhile, it will increase the impact degree, which affects the safe operation of rotating machines to a great extent.

When dealing with the rub-impact between the blades and the casings, the initial gap between

them is one of the factors that cannot be ignored. At the end of this subsection, the influence of initial gap on the dynamic response of the dual-rotor under rub-impact is investigated.

According to the above analysis, it can be known that the rub-impact fault mainly occurs in the LP rotor at low rotational speed. Therefore, in the process of studying the initial gap, the dynamic variation of the LP rotor is mainly discussed. When the rotational speeds of the LP and HP rotors are $\omega_L = 200$ rad/s and $\omega_H = 240$ rad/s, the initial gap of the dual-rotor system is reset to $\delta_{L0} = \delta_{H0} = [0.05,\ 0.035,\ 0.025,\ 0.01]$ mm. Through the numerical simulation, the impact force and the whirling orbits of the LP rotor in the four cases of initial gap are obtained, as shown in Figs. 24 and 25.
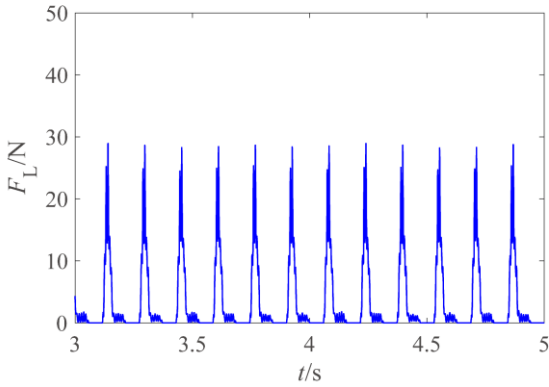

(a) LP rotor without pedestal looseness

(b) HP rotor without pedestal looseness

(c) LP rotor with pedestal looseness

(d) HP rotor with pedestal looseness

Fig. 23 Whirling orbits of the dual-rotor system at $\omega_L = 300$ rad/s and $\omega_H = 360$ rad/s: (a) LP rotor without pedestal looseness, (b) HP rotor without pedestal looseness, (c) LP rotor with pedestal looseness, and (d) HP rotor with pedestal looseness.
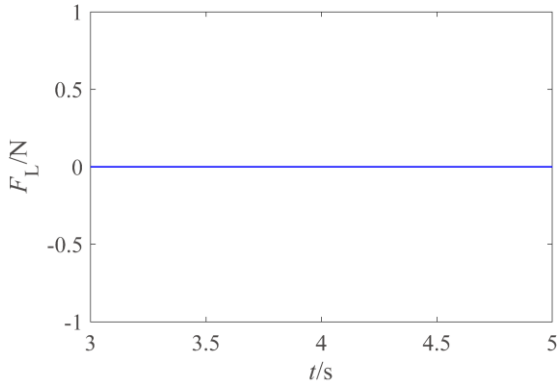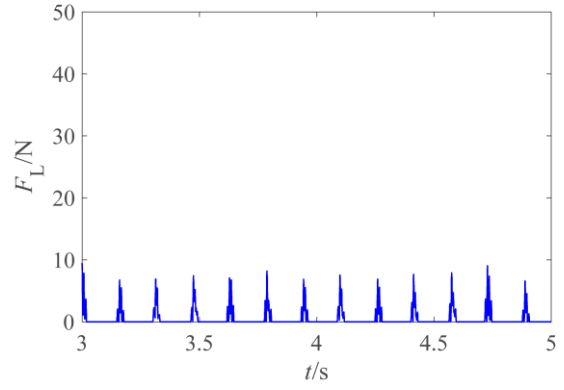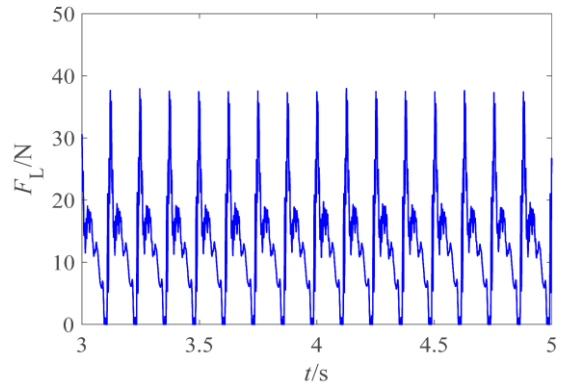
Fig. 24 Impact force of LP rotor in the different condition of initial gap: (a) $\delta_{L0}=\delta_{H0}=0.05$ mm, (b) $\delta_{L0}=\delta_{H0}=0.035$ mm, (c) $\delta_{L0}=\delta_{H0}=0.025$ mm, and (d) $\delta_{L0}=\delta_{H0}=0.01$ mm.
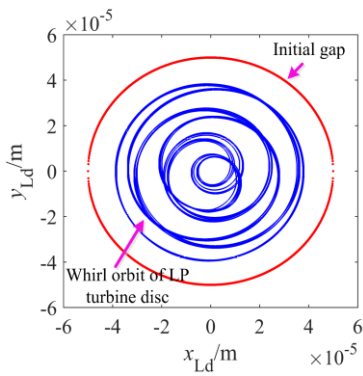
(c) $\delta_{L0}=\delta_{H0}=0.025$ mm   (d) $\delta_{L0}=\delta_{H0}=0.01$ mm

Fig. 25 Whirling orbits of the LP turbine disc in the different condition of initial gap: (a) $\delta_{L0}=\delta_{H0}=0.05$ mm, (b) $\delta_{L0}=\delta_{H0}=0.035$ mm, (c) $\delta_{L0}=\delta_{H0}=0.025$ mm, and (d) $\delta_{L0}=\delta_{H0}=0.01$ mm.
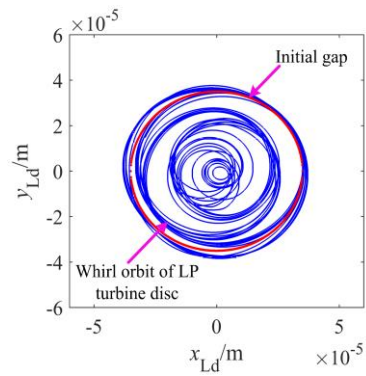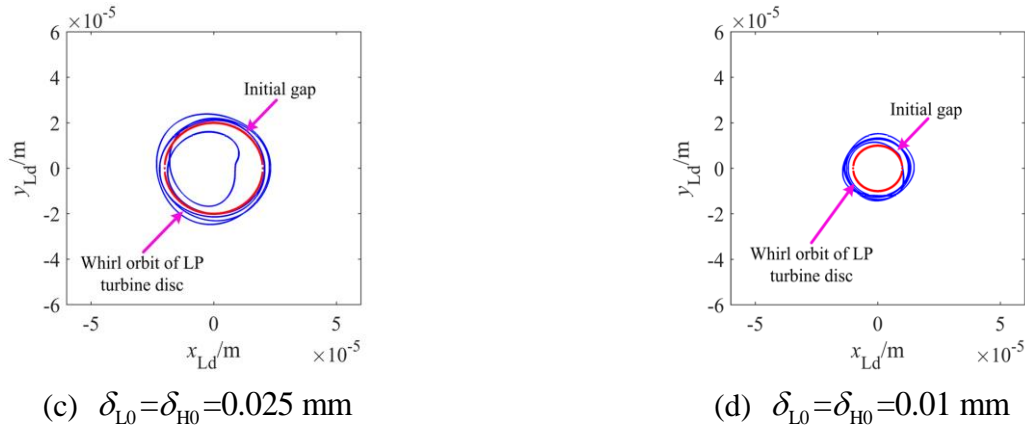
Obviously, with the decrease of initial gap, the impact force of the LP rotor increases gradually. Meanwhile, more collisions between the blade and the casing will occur in the same time interval. From the view point of whirling orbit, the reduction of the initial gap can lead to the decrease of whirling amplitude of the LP rotor. The main reason is that when rub-impact fault happens, the casing provides the additional constraints on the LP rotor, which greatly limits the motion of the system. However, the probability of blade-casing rub is increased sharply by the tighter initial gap, which may result in decreased machine life and adverse thermal effects.

5. Conclusions

To ensure the smooth operation of rotating machines such as the dual-rotor system of an aero engine, predicting the dynamic performance associated with pedestal looseness fault is of high significance. Based on the structure of a test rig of a dual-rotor-bearing-double casing system, its dynamic model is proposed in this paper, in which a looseness fault occurs on one of the pedestals of the high pressure (HP) rotor. Two imbalance excitations may further lead to the rub-impact between the multi-stage turbine blades and the multi-layer casings. In combination with the distributed soft coating on the outer casing and distributed hard coating on the inner casing, the Lankarani-Nikravesh model and the Coulomb model are adopted to describe the mechanism of rub-impact. According to the experiment performed on the test rig, the vibration behaviours of the dual-rotor system are studied at different rotational speeds, and the particular frequency components caused by blade-casing rub are identified. On this basis, the influences of pedestal looseness and rub-impact on the dynamic characteristics of the dual-rotor system are discussed through numerical simulation. Some conclusions are summarized as follows:

(1) Vibration experiment performed on a rotor test rig proves that the theoretical model for a dual-rotor-bearing-double casing system is valid to some extent.

(2) The speed ratio of LP and HP rotors could directly affect the motion states of the system, leading to periodic motion, quasi-periodic motion and beat vibration. In order to ensure the smooth operation of the system, the rotational speed of the LP and HP rotors should not be close to each other.

(3) Although the pedestal looseness fault only occurs in a local area, its influences may be

global because the pedestal is a central component with the dual-rotor system.

(4) Due to the pedestal looseness and partial rub, impulse responses of the inner and outer casings appear in the time domain. In condition monitoring of rotating machinery, these unique phenomena can be used to judge partial rub and pedestal looseness.

(5) Under the influence of pedestal looseness, rub-impact fault, especially partial rub, is easy to occur in the dual-rotor system. At the same time, the rub-impact magnitude of the dual-rotor system with pedestal looseness tends to be more severe.

(6) When designing the structure of a dual-rotor system, besides the goals of light weight and high thrust, the dynamic stability of the system should also be one. At the same time, the installation position and installation quality of bearing supports are important factors that directly affect the dynamic characteristics of the system.

Acknowledgements

Appendix

Table 1 Main parameters of a dual-rotor-bearing-double casing system [13]

Physical parameter	Variable	Value
Length of LP and HP shaft (mm)	l_L and l_H	706, 501
Outer radius of LP and HP shaft (mm)	R_{Lb} and R_{Hb}	12.5, 20
Inner radius of LP and HP shaft (mm)	r_{Lb} and r_{Hb}	7.5, 15
Elastic modulus of LP and HP shaft (GPa)	E	210
Density of LP and HP shaft (kg/m^3)	ρ	7850
Outer radius of LP and HP disc (mm)	R_{Ld} and R_{Hd}	125
Inner radius of LP and HP disc (mm)	r_{Ld} and r_{Hd}	12.5
Thickness of LP and HP disc (mm)	T_d	27.3
Density of LP and HP disc (kg/m^3)	ρ_d	7850
Eccentricity of LP and HP turbine disc (mm)	e_d	0.01
Mass of inner and outer casing (kg)	m_{ic} and m_{oc}	50
Support stiffness of inner and outer casing (MN/m)	k_{ic} and k_{oc}	2500
Support damping of inner and outer casing (N.s/m)	c_{ic} and c_{oc}	2100
Mass of pedestal (kg)	m_p	10
Stiffness of pedestal without looseness (MN/m)	k_{p2}	250

Damping of pedestal without looseness (N.s/m)	c_{p2}	2100
Mass of bearing outer ring (kg)	m_{br}	2
Stiffness of bearing outer ring (MN/m)	k_{br}	25
Damping of bearing outer ring (N.s/m)	c_{br}	1050
Number of rolling balls	N_r	8
Contact stiffness coefficient of bearing (MN/m$^{3/2}$)	C_b	13340
Initial clearance of rolling bearing (mm)	r_0	0.004
Impact stiffness of LP turbine-outer casing (MN/m$^{3/2}$)	k_L	2500
Friction coefficient of LP turbine-outer casing	μ_L	0.1
Impact stiffness of HP turbine-inner casing (MN/m$^{3/2}$)	k_H	50000
Initial gap of LP turbine-outer casing (mm)	δ_{L0}	0.02
Initial gap of HP turbine-inner casing (mm)	δ_{H0}	0.02
Number of LP and HP blades	N_L and N_H	8

Conflict of interest

We declare that we do not have any commercial or associative interest that represents a conflict of interest in connection with the work submitted.

References

[1] K. Gupta, K.D. Gupta, K. Athre, Unbalance response of a dual rotor system: theory and experiment. J. Vib. Acoust.-Trans. ASME. 115 (1993): 427-435.

[2] Z. Fei, S. Tong, C. Wei, Investigation of the dynamic characteristics of a dual rotor system and its start-up simulation based on finite element method. J. Zhejiang Univ.-SCI. A (Appl Phys & Eng). 14(4) (2013): 268-280.

[3] G. Ferraris, V. Maisonneuve, M. Lalanne, Prediction of the dynamic behavior of non-symmetric coaxial co- or counter-rotating rotors. J. Sound Vib. 195 (4) (1996): 649-666.

[4] D.W. Childs, A modal transient rotordynamic model for dual-rotor jet engine systems. J. Eng. Ind.-Trans. ASME. 98(3) (1976): 876-882.

[5] L. Hou, Y.S. Chen, Y.Q. Fu, H.Z. Chen, Z.Y. Lu, Z.S. Liu, Application of the HB-AFT method to the primary resonance analysis of a dual-rotor system. Nonlinear. Dyn. 88 (2017): 2531-2551.

[6] D.F. Li, E.J. Gunter, A study of the modal truncation error in the component mode analysis of a dual-rotor system. J. Eng. Power. 104 (1982): 525-532.

[7] M. Guskov, J.-J. Sinou, F. Thouverez, O.S. Naraikin, Experimental and numerical investigations

of a dual-shaft test rig with intershaft bearing. Int. J. Rotat. Mach. (2007): 1-12.

[8] A. Anilkumar, V. Kartik, In-plane parametric instability of a rigid body with a dual-rotor system. Proceedings of the ASME 2015 International Mechanical Engineering Congress and Exposition, November 13-19, 2015, Houston, Texas.

[9] P.C. Yu, D.Y. Zhang, Y.H. Ma, J. Hong, Dynamic modeling and vibration characteristics analysis of the aero-engine dual-rotor system with Fan blade out. Mech. Syst. Signal Process. 106 (2018): 158-175.

[10] G.Y. Sun, A. Palazzolo, A. Provenza, C. Lawrence, K. Carney, Long duration blade loss simulation including thermal growths for dual-rotor gas turbine engine. J. Sound Vib. 316 (2008): 147-163.

[11] Z.Y. Lu, L. Hou, Y.S. Chen, C.Z. Sun, Nonlinear response analysis for a dual-rotor system breathing transverse crack in the hollow shaft. Nonlinear. Dyn. 83 (2016): 169-185.

[12] N.F. Wang, D.X. Jiang, Vibration response characteristics of a dual-rotor with unbalance-misalignment coupling faults: Theoretical analysis and experimental study. Mech. Mach. Theory. 125 (2018): 207-219.

[13] Y. Yang, D.Q. Cao, T.H. Yu, D.Y. Wang, C.G. Li, Prediction of dynamic characteristics of a dual-rotor system with fixed point rubbing-Theoretical analysis and experimental study. Int. J. Mech. Sci. 115-116 (2016): 253-261.

[14] Y. Yang, D.Q. Cao, D.Y. Wang, G.Y. Jiang, Fixed-point rubbing characteristic analysis of a dual-rotor system based on the Lankarani-Nikravesh model. Mech. Mach. Theory. 103 (2016): 202-221.

[15] R.S. Srinivas, R. Tiwari, C. Kannababu, Model based analysis and identification of multiple fault parameters in coupled rotor systems with offset discs in the presence of angular misalignment and integrated with an active magnetic bearing. J. Sound Vib. 450 (2019): 109-140.

[16] S. Bab, S.E. Khadem, M. Shahgholi, A. Abbasi, Vibration attenuation of a continuous rotor-blisk-journal bearing system employing smooth nonlinear energy sinks. Mech. Syst. Signal Process. 84 (2017): 128-157.

[17] J. Taghipour, M. Dardel, M.H. Pashaei, Vibration mitigation of a nonlinear rotor system with linear and nonlinear vibration absorbers. Mech. Mach. Theory. 128 (2018): 586-615.

[18] L.D. Hall, D. Mba, Acoustic emissions diagnosis of rotor-stator rubs using the KS statistic. Mech. Syst. Signal Process. 18 (2004): 849-868.

[19] K. Lu, Y.L. Jin, Y.S. Chen, Q.J. Cao, Z.Y. Zhang, Stability analysis of reduced rotor pedestal looseness fault model. Nonlin. Dyn. 82 (2015): 1611-1622.

[20] P.S. Keogh, Contact dynamic phenomena in rotating machines: Active/passive considerations. Mech. Syst. Signal Process. 29 (2012): 19-33.

[21] M.R. Mehrjou, N. Marium, M.H. Marhaban, N. Misron, Rotor fault condition monitoring techniques for squirrel-cage induction machine—A review. Mech. Syst. Signal Process. 25 (2011): 2827-2848.

[22] M. Torkhani, L. May, P. Voinis, Light, medium and heavy partial rubs during speed transients of

rotating machines: Numerical simulation and experimental observation. Mech. Syst. Signal Process. 29 (2012): 45-66.

[23] E. Tofighi-Niaki, P. Asgharifard-Sharabiani, H. Ahmadian, Nonlinear dynamics of a flexible rotor on tilting pad journal bearings experiencing rub-impact. Nonlinear. Dyn. 94 (2018): 2937-2956.

[24] S. Roques, M. Legrand, P. Cartraud, C. Stoisser, C. Pierre, Modeling of a rotor speed transient response with radial rubbing. J. Sound Vib. 329 (2010): 527-546.

[25] N. Harish Chandra, A.S. Sekhar, Fault detection in rotor bearing systems using time frequency techniques. Mech. Syst. Signal Process. 72-73 (2016): 105-133.

[26] B.K. Weaver, Y. Zhang, A.F. Clarens, A. Untaroiu, Nonlinear analysis of rub impact in a three-disk rotor and correction via bearing and lubricant adjustment. J. Eng. Gas Turbines Power. 137(9) (2015): 092504-1-092504-8.

[27] S. Popprath, H. Ecker, Nonlinear dynamics of a rotor contacting an elastically suspended stator. J. Sound Vib. 308 (2007): 767-784.

[28] A.D. Shaw, A.R. Champneys, M.I. Friswell, Normal form analysis of bouncing cycles in isotropic rotor stator contact problems. Int. J. Mech. Sci. 155 (2019): 83-97.

[29] H.F. Wang, G. Chen, Certain type turbofan engine whole vibration model with support looseness fault and casing response characteristics. Shock Vib. (2014): 1-23.

[30] M. Jiang, J.G. Wu, X.S. Peng, X.J. Li, Nonlinearity measure based assessment method for pedestal looseness of bearing-rotor systems. J. Sound Vib. 411 (2017): 232-246.

[31] R.L. Ruhi, T.F. Conry, R.L. Steger, Unbalanced response of a large rotor-pedestal-foundation system using an elastic half-space soil model. J. Mech. Des. 102(2) (1980): 311-319.

[32] Z.Y. Qin, Q.K. Han, F.L. Chu, Bolt loosening at rotating joint interface and its influence on rotor dynamics. Eng. Fail. Anal. 59 (2016): 456-466.

[33] M. Nataraj, G. Baskaran, Experimental investigation of misalignment and looseness in rotor bearing system using Bartlett power spectral density. J. Sci. Ind. Res. 76 (2017): 308-313.

[34] A. Muszynska, Rotordynamic. CRC Press. 1st Edition. 2015.

[35] G. Chen, C.G. Li, D.Y. Wang, Nonlinear dynamic analysis and experiment verification of rotor-ball bearings-support-stator coupling system for aeroengine with rubbing coupling faults. J. Eng. Gas Turbine Power. 132(2) (2009): 022501-1-022501-9.

[36] T.N. Rhys-Jones, Thermal sprayed coating systems for surface protection and clearance control applications in aero engines, Surf. Coat. Technol. 43/44 (1990): 402-415.

[37] D. Maraini, C. Nataraj, Nonlinear analysis of a rotor-bearing system using describing functions. J. Sound Vib. 420 (2018): 227-241.

[38] T.A. Harris, M.N. Kotzalas, Essential concepts of bearing technology. CRC Press Boca Raton. 2006.

[39] H. Ma, X.Y. Zhao, Y.N. Teng, B.C. Wen, Analysis of dynamic characteristics for a rotor system with pedestal looseness. Shock Vib. 18(1) (2011): 13-27.

[40] H.M. Lankarani, P.E. Nikravesh, A contact force model with hysteresis damping for impact analysis of multibody systems. ASME J. Mech. Des. 112 (1990): 369-376.

[41] J.P. Den Hartog, Forced vibrations with combined coulomb and viscous friction. Trans. ASME APM. 53-9 (1931): 107-115.

[42] Y. Yang, D.Q. Cao, D.Y. Wang, G.Y. Jiang, Response analysis of a dual-disc rotor system with multi-unbalances-multi-fixed-point rubbing faults. Nonlinear Dyn. 87(1) (2017): 109-125.